

Master's Thesis

**Multifunctional Natural Polysaccharides  
for Energy Storage Applications**

Gaeun Hwang

Department of Energy Engineering  
(Battery Science and Technology)

Graduate School of UNIST

2015

# Multifunctional Natural Polysaccharides for Energy Storage Applications

Gaeun Hwang

Department of Energy Engineering  
(Battery Science and Technology)

Graduate School of UNIST

# Multifunctional Natural Polysaccharides for Energy Storage Applications

A thesis  
submitted to the Graduate School of UNIST  
in partial fulfillment of the  
requirements for the degree of  
Master of Science

Gaeun Hwang

6. 18. 2015

Approved by



---

Advisor

Soojin Park

# Multifunctional Natural Polysaccharides for Energy Storage Applications

Gaeun Hwang

This certifies that the thesis of Gaeun Hwang is approved.

6. 18. 2015

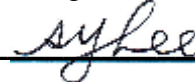
Signature



---

Thesis supervisor: Soojin Park

Signature



---

Sang-Young Lee

Signature



---

Kwanyong Seo

## Abstract

An agarose is a polysaccharide material, generally extracted from seaweeds. Agarose is a linear polymer made up of the repeating unit of agarobiose, which is a disaccharide made up of D-galactose and 3,6-anhydro-L-galactopyranose. Many applications of agarose are described in the literature from biology to energy field, such as gel electrophoresis, protein purification, solid culture media, motility assays, template for the fabrication of porous structures, binder, separator membrane, and carbon-coating material for lithium-ion batteries (LIBs).

Silicon (Si) has attracted much attention as promising anode material due to its high theoretical capacity (3579 mA h g<sup>-1</sup> with composition of Li<sub>15</sub>Si<sub>4</sub> at room temperature), relatively low working potential (< 0.4 versus Li/Li<sup>+</sup>), its abundance in nature, and low cost.<sup>7-10</sup> However, the large volume change of Si (> 300% with composition of Li<sub>3.75</sub>Si at room temperature) during lithiation/delithiation leads to a serious aggregation of Si, the formation of unstable thick solid-electrolyte-interface (SEI) layers and depletion of electrolyte, which will make critical capacity fading. Furthermore, Si has low electrical conductivity and sluggish lithium-ion diffusivity. These fatal flaws prevent the commercialization of Si anode. There are several solutions to overcome these drawbacks, including Si composites with metal oxide, inactive metals, or carbon materials and Si nanostructuring (e.g., nanoparticles, nanowires, and nanotubes). Another attempt has been tried to develop functional polymeric binders which can alleviate severe volume change of Si anodes. Actually, overall quality of batteries depends on performance of binders, because polymeric binders give adhesion between electrode and current collector, allowing long-term cycling stability. Natural polysaccharide was used as polymeric binder for Si anodes, because it contains many functional groups, which are expected to generate strong adhesion between binder and active material.

In chapter II, we demonstrate eco-friendly, abundant natural polysaccharide as a binder for Si-based anode, Si/C composite materials consisting of the Si foam dispersed in hard carbon (HC) synthesized by using agarose, and LiMn<sub>2</sub>O<sub>4</sub> cathodes. Si foam@HC@C was successfully synthesized by a simple carbonization method. The nanostructured Si foam and agarose binder containing many functional groups enables to strong adhesion between Si foam and current collector, leading to enhanced electrochemical properties, including a high specific capacity of 1028 mAh g<sup>-1</sup> (60% retention compared to 2<sup>nd</sup> cycle) and outstanding cycling performance after 200 cycles. Si foam@HC@C electrode showed first discharge capacity and discharge capacity were 654 and 513 mAh g<sup>-1</sup> with enhanced initial coulombic efficiency of 78.4%, compared to HC@C with initial coulombic efficiency of 71.6%. LiMn<sub>2</sub>O<sub>4</sub> cathode with agarose binder exhibited high initial coulombic efficiency of 96.2% and stable cycling performance with nearly 100% coulombic efficiency. These results indicate agarose binder can

be used for both of anode and cathode due to good electrochemical stability in wide operating voltage.

In chapter III, Si/Al<sub>2</sub>O<sub>3</sub> foam particles were simply synthesized by the chemical etching of the Al–Si alloy and a subsequent selective thermal oxidation process. The Si/Al<sub>2</sub>O<sub>3</sub> electrodes with tunable Al<sub>2</sub>O<sub>3</sub> thickness exhibited highly stable cycling performance, excellent rate capability, and suppressed volume expansion. This strategy opens up an effective way to introduce various protecting layers on the surface of other inorganic materials.



## Contents

Abstract .....	1
List of Figures .....	6
List of Tables .....	9
Chapter I. Introduction .....	10
1. Natural Polysaccharides .....	10
1.1 Structure and properties of agar/agarose .....	13
1.2 Extraction method of agar .....	14
1.3 Application of agar/agarose .....	16
1.4 References .....	18
2. Lithium-Ion Batteries .....	20
2.1 Basic Principles of Lithium-Ion Batteries .....	21
2.2 Components in Lithium-Ion Batteries .....	23
2.2.1 Cathode materials .....	26
2.2.2 Anode materials .....	29
2.2.3 Separators .....	33
2.2.4 Electrolytes .....	35
2.3 References .....	36
Chapter II. Multifunctional Natural Polysaccharide Binder for Lithium-Ion Battery Anodes .....	39
1. Introduction .....	39
2. Experimental .....	41
2.1 Synthesis of Si foam @ Hard Carbon (HC) @ C .....	41
2.2 Characterization .....	41
2.3 Electrochemical measurements .....	42
3. Results and discussion .....	43
3.1. Preparation of nanostructured Si foam and its electrochemical test using agarose binder .....	43
3.2. Preparation of HC@C and Si foam@HC@C and its electrochemical test using agarose binder .....	48
3.3. Electrochemical performance of LiMn <sub>2</sub> O <sub>4</sub> cathode with agarose binder .....	51
4. Conclusion .....	51



5. References .....	53
---------------------	----

Chapter III. A High-performance Nanoporous Si/Al<sub>2</sub>O<sub>3</sub> Foam Lithium-Ion Battery Anode Fabricated by Selective Chemical Etching of the Al-Si Alloy and Subsequent Thermal Oxidation .....

1. Introduction .....	56
2. Experimental .....	58
2.1 Synthesis of Si/Al <sub>2</sub> O <sub>3</sub> Foam .....	58
2.2 Characterization .....	58
2.3 Electrochemical measurements .....	58
3. Results and discussion .....	60
4. Conclusion .....	77
5. References .....	78

## List of figures

**Figure 1.1.1.** Skeletal formula of glucose and some polysaccharides.

**Figure 1.1.2.** Method of extraction of agar from seaweed.

**Figure 1.1.3.** Applications of Agarose.

**Figure 1.2.1.** Schematic of the principle of operation of commercial LIBs in which Li ions move from negative electrode to the positive electrode during discharge and back when charging.

**Figure 1.2.2.** Cost Estimation of Lithium-Ion Batteries.

**Figure 1.2.3.** The three types of Anode Materials for LIBs.

**Figure 2.1.** Characterization of Si foam. SEM images of (a) pristine Al-Si powder and (b) Si foam (inset: TEM image of Si foam with Si frame in range of 50–100 nm.) (c) TEM image and (d) XRD pattern of Si foam. (e) Nitrogen adsorption and desorption isotherm and (f) pore size distribution of Si foam.

**Figure 2.2.** Peel-off test of PVdF and Agarose binder on Si wafer after spin coating for 2 min at 2000rpm.

**Figure 2.3.** (a) FT-IR spectra of agarose film, Si foam powder, and electrode consisted of Si foam and agarose. (b) Stress-strain curves of agarose film and PVdF film.

**Figure 2.4.** Electrochemical performance of Si foam using agarose binder and PVdF binder. (a) First cycle voltage profiles in range of 0.005-1.5 V at a rate of C/20. (b) Cycling performance in range of 0.01-1.2V at a rate of 0.2C.

**Figure 2.5.** SEM images of (a) as-synthesized HC@C and (b) Si foam@HC@C. (c) XRD pattern of HC@C and Si foam@HC@C. (Inset: TEM images of HC@C and Si foam@HC@C.) (d) TGA analysis of Si foam@HC@C. This result shows Si foam@HC@C contains 85 wt% of carbon and 15 wt% of

silicon.

**Figure 2.6.** Electrochemical performance of HC@C and Si foam@HC@C electrodes. (a) First cycle voltage profiles obtained at the C/20 rate between 0.005V and 2.0V. Cycle performance of HC@C and Si foam@HC@C at rate of (a) 0.2C and (c) 1C discharge/charge. (d) Rate capability of HC@C and Si foam@HC@C electrodes in the range of C/5-15C (same discharge/charge rate).

**Figure 2.7.** (a) First charge and discharge voltage profile in voltage range of 3-4.3V at rate of C/20. (b) Cycling stability test in range of 3-4.3V at 0.2C/0.2C (charge/discharge).

**Figure 3.1.** (a) Schematic illustration showing the synthetic process of Al-Si foam-like particles. SEM images of (b) pristine Al-Si alloy and (c) chemically etched Al-Si powder. XRD patterns of (d) Al-Si alloy and (e) chemically etched Al-Si powder.

**Figure 3.2.** EDS spectra of (a) Al-Si alloy powder and (b) chemically etched Al-Si powder.

**Figure 3.3.** SEM images of chemically etched Al-Si particles for (a) 10 min, (b) 30 min, (c) 45 min, and (d) 60 min at room temperature.

**Figure 3.4.** (a) Schematic illustration showing the thermal oxidation process of chemically etched Al-Si particles. HAADF-STEM and the corresponding EDS mapping images of (b) etched Al-Si powder and (c) thermally oxidized (10 min) Al-Si powder.

**Figure 3.5.** SEM images and EDS spectra of (a) chemically etched Al-Si powder and Si/Al<sub>2</sub>O<sub>3</sub> particles thermally oxidized for (b) 10 min, (c) 30 min, and (d) 60 min.

**Figure 3.6.** XRD patterns of chemically etched Al-Si and three different thermally oxidized Al-Si powders.

**Figure 3.7.** TEM images of thermally oxidized samples at 600 °C: Thermally oxidized Si for (a) 10 min, (b) 30 min, (c) 60 min and (d) thermally oxidized Al sample for 10 min. In the case Al particle, we used micrometer-sized Al (an average particle size of 3 μm). After thermal oxidation at 600 °C for 10 min, a focused-ion beam technique was employed to obtain sectioned sample for TEM measurement.

**Figure 3.8.** XRD patterns of pure Al and samples thermally oxidized at 600 °C for 10 min (red), 30

min (blue), and 60 min (cyan). As the oxidation time increased, the Al peak was gradually decreased. From the first order scattering peak of each sample, we estimated the  $\text{Al}_2\text{O}_3$  contents from the Al contents remained after the thermal oxidation. When the pure Al was thermally oxidized for 10 min, 30 min, and 60 min, the  $\text{Al}_2\text{O}_3$  layers of 20%, 25%, and 35% were formed on the Al surface, respectively. It should be noted that the Al of 65% was still left, even though the pure micrometer-sized Al particles was oxidized at 600 °C for 60 min.

**Figure 3.9.** BET surface area of (a) pristine Al-Si alloy, (b) 30 min-etched Al-Si, and (c) 10 min thermally oxidized Si/ $\text{Al}_2\text{O}_3$ . (d) Pore size distribution of the chemically etched and 10 min oxidized particles.

**Figure 3.10.** Electrochemical performances of etched Al-Si and thermally oxidized (10, 30, and 60 min) Si/ $\text{Al}_2\text{O}_3$  electrode. (a) First cycle voltage profiles obtained at the C/20 rate and (b) cycling performances at the C/5 rate for four Si-based electrodes. (c) Long-term cycling stability of the thermally oxidized (10 min) Si/ $\text{Al}_2\text{O}_3$  electrode. (d) Rate capabilities of four Si-based electrodes obtained in the range of C/5–10C (the lithiation rate was fixed at C/5).

**Figure 3.11.** Electrochemical impedance spectra of chemically etched Al-Si and Si/ $\text{Al}_2\text{O}_3$  electrodes thermally oxidized for 10, 30 and 60 min (a) after 1st cycle (b) after 120th cycle.

**Figure 3.12.** Rate capabilities of chemically etched Al-Si and Si/ $\text{Al}_2\text{O}_3$  electrodes thermally oxidized for 10, 30, and 60 min. The Li extraction rate was fixed at C/5 and Li insertion rate was varied from C/5 to 10C.

**Figure 3.13.** Cross-sectional SEM images of electrode before and after cycle. (a) Chemically etched Al-Si electrode after 124th cycle and Si/ $\text{Al}_2\text{O}_3$  electrodes thermally oxidized for (b) 10 min, (c) 30 min, and (d) 60 min after 150th cycle.

**Figure 3.14.** SEM images of (a) 30 min-chemically etched Al-Si powder before and (b) after 120 cycles. Inset shows the corresponding TEM image of Al-Si frame before and after cycle. SEM images of 10 min-oxidized Si/ $\text{Al}_2\text{O}_3$  particles (c) before and (b) after 120 cycles. The corresponding TEM image of Si/ $\text{Al}_2\text{O}_3$  frame was seen in the inset before and after cycle.

## List of tables

**Table 1.1.1.** Structures and Roles of Some Polysaccharides.

**Table 1.2.1.** Components and examples of materials of Lithium-Ion Batteries.

**Table 1.2.2.** Electrochemical Characteristics of Various types of Cathode materials.

**Table 1.2.3.** Main characteristics of common anode active materials.

**Table 1.2.4.** Requirements for Separators.

**Table 3.1.** EDS data of the amount of elements depending on etching time.

## Chapter I. Introduction

### 1. Natural Polysaccharides

Polysaccharides are polymeric carbohydrate molecules composed of hundreds or thousands of long chains of monosaccharide units bound together by glycosidic linkages and give the constituent monosaccharides or oligosaccharides on hydrolysis. Their structures are varied from linear to highly branch. Polysaccharides can be classified into roughly two types, including storage polysaccharides such as starch and glycogen, and structural polysaccharides such as cellulose, chitin, dextran, and agarose. Structures and roles of some polysaccharides are displayed in Table 1.1.

Polysaccharides are often quite heterogeneous containing slight modifications of the repeating unit. Depending on the structure, these macromolecules can have distinct properties from their monosaccharide building blocks. They are amorphous or even insoluble in water. When all the monosaccharides in a polysaccharide are the same type, the polysaccharide is called a homopolysaccharide or homoglycan. Meanwhile, when more than one type of monosaccharide is present they are called heteropolysaccharides.

Natural saccharides are generally of simple carbohydrates called monosaccharides with general formula  $(\text{CH}_2\text{O})_n$  where  $n$  is three or more. Examples of monosaccharides are glucose, fructose, and glyceraldehyde. Fig 1.1 illustrates skeletal formula of glucose and some structural polysaccharide. Polysaccharides have a general formula of  $\text{C}_x(\text{H}_2\text{O})_y$  where  $x$  is usually a large number between 200 and 2500. Considering that the repeating units in the polymer backbone are often six-carbon monosaccharides, the general formula can also be represented as  $(\text{C}_6\text{H}_{10}\text{O}_5)_n$  where  $40 \leq n \leq 3000$ .

Cellulose, chitin, dextran, agarose are of structural polysaccharides. Cellulose is used in the cell walls of plants and other organisms, and is said to be the most abundant organic molecule on earth. It has many uses such as a significant role in the paper and textile industries, and is used as a feedstock for the production of rayon (via the viscose process), cellulose acetate, celluloid, and nitrocellulose. Chitin has a similar structure, but has nitrogen-containing side branches, increasing its strength. It is found in arthropod exoskeletons and in the cell walls of some fungi. It also has multiple uses, including surgical threads. Dextran was first discovered by Louis Pasteur as a microbial product in wine. It is used medicinally as an antithrombotic, to reduce blood viscosity, and as a volume expander in hypovolaemia. Agarose is generally extracted from seaweed. It is frequently used in molecular biology for the separation of large molecules, especially DNA, by electrophoresis.<sup>1-4</sup>

**Table 1.1.1.** Structures and Roles of Some Polysaccharides.

<b>Polymer</b>	<b>Type*</b>	<b>Size (number of monosaccharide units)</b>	<b>Roles/significance</b>
Starch	Homo-	50-5,000 Up to 10 <sup>6</sup>	Energy storage: in plants
Glycogen	Homo-	Up to 50,000	Energy storage: in bacteria and animal cells
Cellulose	Homo-	Up to 15,000	Structural: in plants, gives rigidity and strength to cell walls
Chitin	Homo-	Very large	Structural: in insects, spiders, crustaceans, gives rigidity and strength to exoskeletons
Dextran	Homo-	Wide range	Structural: in bacteria, extracellular adhesive
Agarose	Hetero-	1,000	Structural: in algae, cell wall material

\*Each polymer is classified as a homopolysaccharide (homo-) or heteropolysaccharide (hetero-).

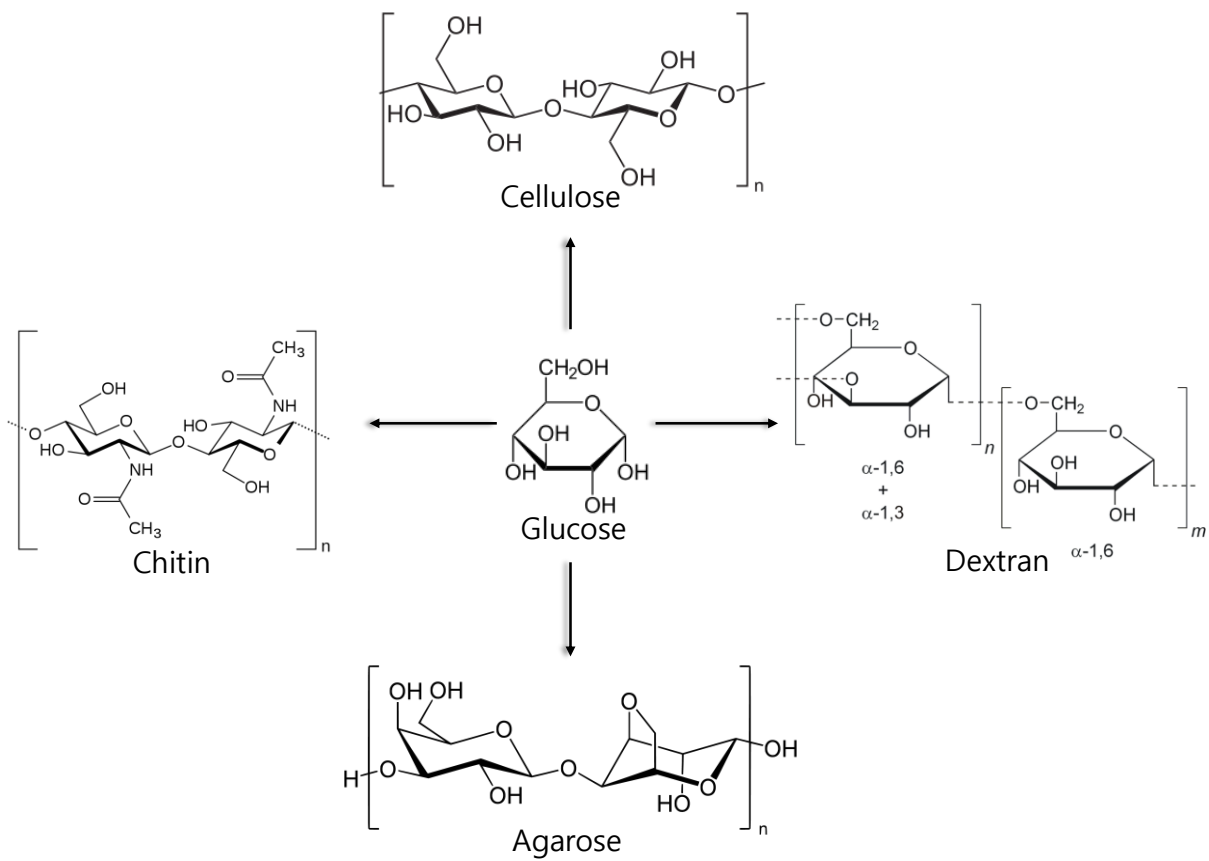


**Figure 1.1.1.** Skeletal formula of glucose and some polysaccharides.



## 1.1. Structure and properties of agar/agarose

An agarose is a polysaccharide material, generally extracted from seaweeds. Agarose is a linear polymer made up of the repeating unit of agarobiose, which is a disaccharide made up of D-galactose and 3,6-anhydro-L-galactopyranose. Agarose is one of the two principal components of agar, and is purified from agar by removing agar's other component, agarpectin. Agar has been known for its gelling properties since the 17<sup>th</sup> century in Japan. Temperature of gelation, gel strength, composition and yield of polysaccharide extracted depend on the season, solar irradiation, and the algae species.

Agarose is available as a white powder which dissolves in near-boiling water, and forms a gel when it cools. Agarose exhibits the phenomenon of thermal hysteresis in the liquid-to-gel transition, i.e. it gels and melts at different temperatures. The gelling and melting temperature varies depending on the type of agarose. Standard agaroses derived from *Gelidium* has a gelling temperature of 34 – 38 °C and a melting temperature of 90 – 95 °C, while those derived from *Gracilaria*, due to its higher methoxy substituents, has a higher gelling temperature of 40 – 52 °C and melting temperature of 85 – 90 °C. The melting and gelling temperature may be dependent on the concentration of the gel, particularly at low gel concentration of less than 1%. The gelling and melting temperature is therefore given at a specified concentration.

Natural agarose contains uncharged methyl groups and the extent of methylation is directly proportional to the gelling temperature. Synthetic methylation however have the reverse effect, whereby increased methylation lowers the gelling temperature. A variety of chemically modified agaroses with different melting and gelling temperatures are available; these are often made by hydroxyethylation of agarose.

On standing the agarose gels are prone to syneresis (extrusion of water through the gel surface), but the process is slow enough to not interfere with the use of the gel.

Agarose gel can have high gel strength at low concentration, making it suitable as an anticonvection medium for gel electrophoresis. Agarose gels as dilute as 0.15% can form slab for gel electrophoresis. The agarose polymer contains charged groups, in particular pyruvate and sulfate. These negative charged groups can retard the movement of DNA in a process called electroendosmosis (EEO), and low EEO agarose is therefore generally preferred for use in agarose gel electrophoresis of nucleic acids.

Agarose has a single or double helical conformation in the solid state; different types of helical structure were predicted by molecular modelling. Gelation occurs from aggregation of double helices at a temperature which depends on methoxyl and sulfate contents which can modulate gelation. This three-dimensional network based on association of double helices is a physical gel stabilized by cooperative hydrogen bonds. A more recent study interpreted the behavior near the sol–gel transition in terms of percolation. The mechanism of gel formation and essential properties will be described in

comparison with the gelation of  $\kappa$ - and  $\iota$ -carrageenans. The mechanism of gelation is the formation of double helices followed by a phase separation to form a gel. The gels are turbid due to the high degree of helix aggregation directly in relation to the width of the hysteresis. Stronger gels are obtained with purer agarose. These gels show syneresis (separation of water on ageing) corresponding to the slow organization of the double helices in a solid-like material. This gelation and conformational change can also be characterized by calorimetry. The enthalpy for conformational change (and dissociation of helix aggregates)  $H$  was found to be nearly independent of the polymer concentration.

Agar at near neutrality is compatible with most proteins and other polysaccharides. When agarose is mixed with  $\kappa$ -carrageenan, it was shown that the two polymers form independent gels (interpenetrating network).<sup>5</sup>

## **1.2. Extraction method of agar**

Figure 1.2 summarizes the method of extraction of agar from seaweeds. The seaweed is washed and cleaned with water. For gelidium (thalloid algae), it is heated with very dilute acid for 1 hour to improve water penetration. And for gracilaria (red algae), it is treated with alkali and washed.

The extraction of agar is performed from boiled seaweed; the extract is then frozen and thawed. During this last step, water separates from agar carrying with it soluble impurities. Washing, bleaching, sterilization and drying are performed depending on the applications. Treatment in the presence of alkali increases the gel strength by formation of 3,6-anhydrogalactose.

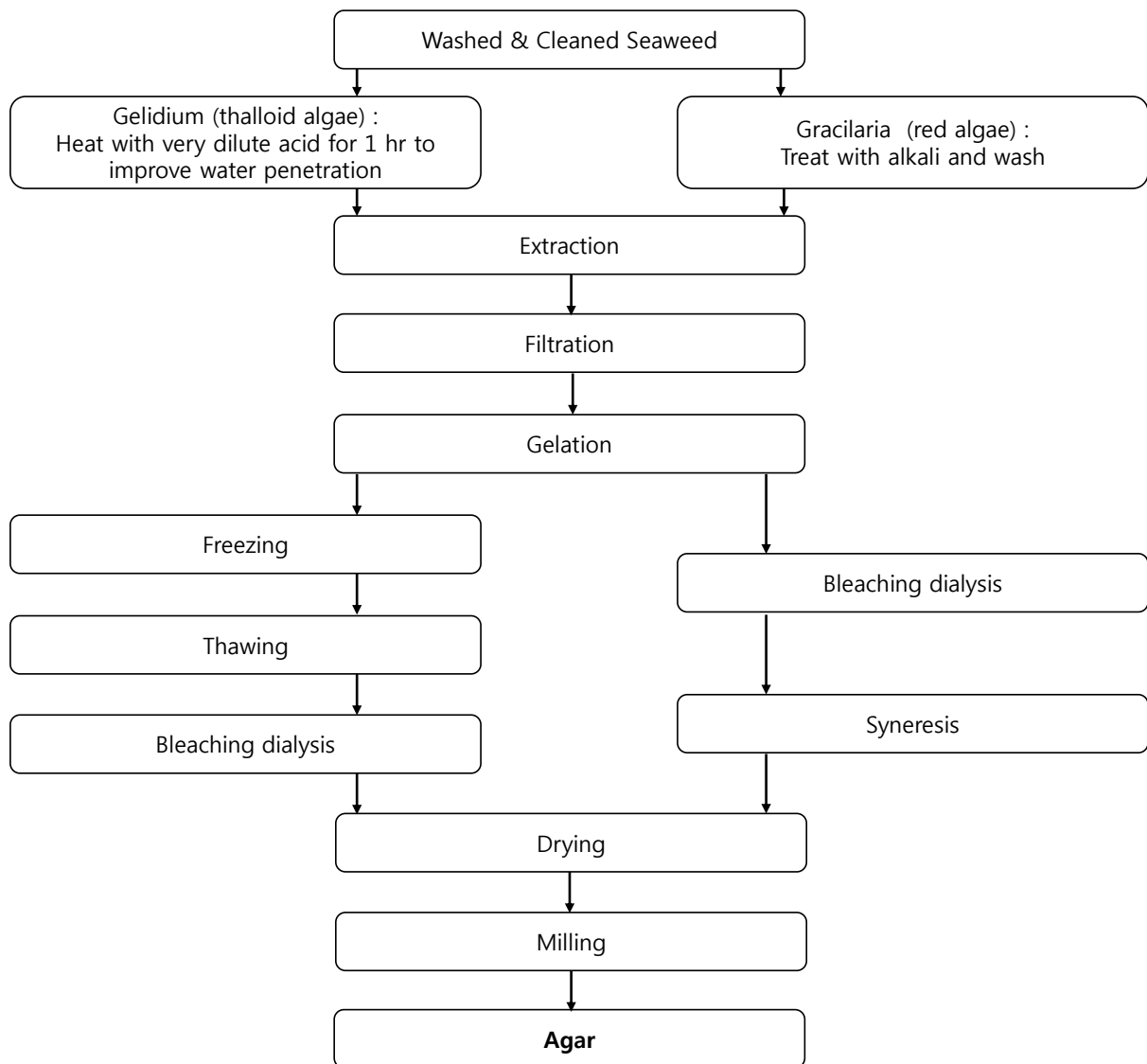


**Figure 1.1.2.** Method of extraction of agar from seaweed.

### 1.3. Applications of agar/agarose

Many applications of agarose and agar are described in the literature from biology to energy field. Fig 1.3. illustrates applications of agarose such as gel electrophoresis<sup>6-8</sup>, protein purification<sup>9</sup>, solid culture media<sup>10,11</sup>, motility assays<sup>12</sup>, template for the fabrication of porous structures<sup>13</sup>, binder, separator membrane, and carbon-coating material for lithium-ion batteries (LIBs)<sup>14-17</sup>.

Agarose is frequently used in molecular biology for the separation of large molecules, especially DNA, by electrophoresis. Slabs of agarose gels (usually 0.7 – 2 %) for electrophoresis are readily prepared by pouring the warm, liquid solution into a mold. A wide range of different agaroses, of varying molecular weights and properties are commercially available for this purpose.

Furthermore, agarose is also used pharmaceuticals, separation and purification media for fine chemicals, hormones, enzymes, vaccines. It can be processed by extrusion from solution at high temperature, forming gel beads into ice-cold buffer. Another technique is to emulsify agarose in a warm fluid which is immiscible with the aqueous polysaccharide solution. Emulsion is produced which is then cooled to get microspheres. It is also widely used as growth medium for microorganisms (bacteria and fungi) and for biotechnological applications. In the food industry soft gels are preferred (agar with some substituents) while the pharmaceutical and microbiological industries prefer a harder gel (i.e., made with the best agarose).

In the domain of biomaterials, the most important application is in tissue engineering and to encapsulate cells (islets of Langerhans, chondrocytes, etc.).

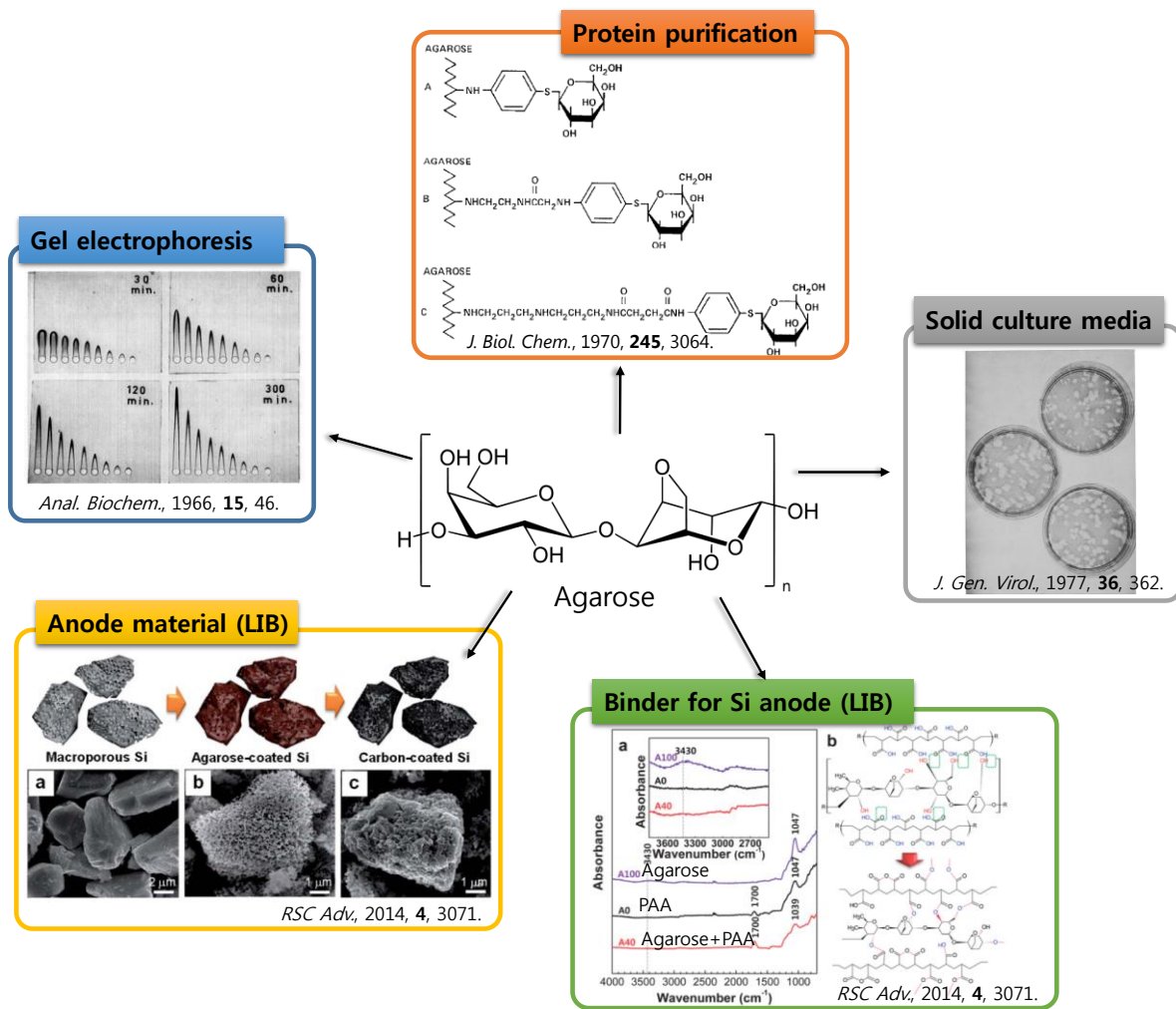


Figure 1.1.3. Applications of Agarose.

#### 1.4. References

1. M. A. Meyers, P.-Y. Chen, A. Y.-M. Lin and Y. Seki, Biological materials: Structure and mechanical properties. *Prog. Mater Sci.* **2008**, *53* (1), 1-206.
2. M. Rinaudo, Chitin and chitosan: Properties and applications. *Prog. Polym. Sci.* **2006**, *31* (7), 603-632.
3. T. M. P. K. K.M.Manjanna, B. Shivakumar, NATURAL POLYSACCHARIDE HYDROGELS AS NOVEL EXCIPIENTS FOR MODIFIED DRUG DELIVERY SYSTEMS: A REVIEW. *International journal of chemtech research* **2010**, *2* (1), 509-525.
4. T. H. Dieter Klemm, *Polysaccharides*, Springer, Berlin Heidelberg, 2006.
5. M. Rinaudo, Main properties and current applications of some polysaccharides as biomaterials. *Polym. Int.* **2008**, *57* (3), 397-430.
6. C.-B. Laurell, Quantitative Estimation of Proteins by Electrophoresis in Agarose Gel Containing Antibodies. *Anal. Biochem.* **1966**, *15* (1), 45-52.
7. A. C. P. a. C. W. Dingman, Molecular Weight Estimation and Separation of Ribonucleic Acid by Electrophoresis in Agarose-Acrylamide Composite Gels. *Biochemistry (Moscow)* **1968**, *7* (2), 668-674.
8. B. A. Sanderson, N. Araki, J. L. Lilley, G. Guerrero and L. K. Lewis, Modification of gel architecture and TBE/TAE buffer composition to minimize heating during agarose gel electrophoresis. *Anal. Biochem.* **2014**, *454*, 44-52.
9. P. Cuatrecasas, Protein Purification by Affinity Chromatography derivatizations of agarose and polyacrylamide beads. *J. Biol. Chem.* **1970**, *245* (12), 3059-3065.
10. M. Brown, and Peter Faulkner, A Plaque Assay for Nuclear Polyhedrosis Viruses using a Solid Overlay. *J. Gen. Virol.* **1977**, *36* (2), 361-364.
11. D. B. Johnson, Selective solid media for isolating and enumerating acidophilic bacteria. *J. Microbiol. Methods* **1995**, *23* (2), 205-218.
12. C. R. D. Lauffenburger, and S. H. Zigmond, MEASUREMENT OF LEUKOCYTE MOTILITY AND CHEMOTAXIS PARAMETERS WITH A LINEAR UNDER-AGAROSE MIGRATION ASSAY. *J. Immunol.* **1983**, *131* (2), 940-947.
13. M. Z. Jingfang Zhou, and Rachel A. Caruso, Agarose Template for the Fabrication of Macroporous Metal Oxide Structures. *Langmuir* **2006**, *22*, 3332-3336.
14. C. Kim, J. Y. Jang, N.-S. Choi and S. Park, Multi-functionalities of natural polysaccharide for enhancing electrochemical performance of macroporous Si anodes. *RSC Adv.* **2014**, *4* (6), 3070.
15. J.-M. Kim, C. Kim, S. Yoo, J.-H. Kim, J.-H. Kim, J.-M. Lim, S. Park and S.-Y. Lee, Agarose-biofunctionalized, dual-electrospun heteronanofiber mats: toward metal-ion chelating battery

- separator membranes. *J. Mater. Chem. A* **2015**, *3* (20), 10687-10692.
16. C. Kim, M. Ko, S. Yoo, S. Chae, S. Choi, E. H. Lee, S. Ko, S. Y. Lee, J. Cho and S. Park, Novel design of ultra-fast Si anodes for Li-ion batteries: crystalline Si@amorphous Si encapsulating hard carbon. *Nanoscale* **2014**, *6* (18), 10604-10610.
17. G.-P. Kim, S. Park, I. Nam, J. Park and J. Yi, Preferential growth of Co<sub>3</sub>O<sub>4</sub> anode material with improved cyclic stability for lithium-ion batteries. *J. Mater. Chem. A* **2013**, *1* (12), 3872.

## 2. Lithium-Ion Batteries

Electrical energy storage (EES) refers to a process converting electrical energy from a power into a form that can be stored for converting back to electrical energy when needed. There are many types of EES system such as pumped hydroelectric storage (PHS), compressed air energy storage (CAES), batteries (lead acid, nickel cadmium, sodium sulfur, sodium nickel chloride, lithium-ion), fuel cell (hydrogen, direct-methanol, molten carbonate, solid oxide fuel cell, metal-air battery), flow battery (vanadium redox, zinc bromine, polysulfide bromide), solar fuels, superconducting magnetic energy storage (SMES), flywheel, capacitor/supercapacitor, thermal energy storage (low-temperature, high-temperature TES).<sup>1-3</sup>

Among these energy storage systems, lithium-ion battery (LIB) is one of the most powerful energy storage devices using for portable electronic devices, electric vehicles, and large-scale energy storage systems due to their light weight (specific gravity of  $0.53 \text{ g cm}^{-3}$ ), high power and high energy density. Moreover, Li has high specific capacity ( $3860 \text{ mA kg}^{-1}$ ) and high electropositive nature (3.4 V versus standard hydrogen electrode) to operate at higher voltages.<sup>4</sup>

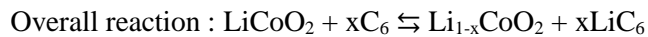
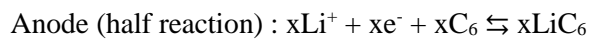
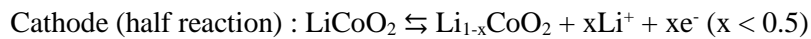
Lithium-ion batteries (LIBs) were first suggested by M.S. Whittingham who are working Exxon company in the 1970s.<sup>5</sup> Whittingham has used titanium sulfide as cathode and lithium metal as anode material and lithium perchlorate in dioxolane electrolyte. Because lithium is a highly reactive with the presence of water and oxygen, lithium metal electrodes have critical safety issues. As a result, researches have focused on developing lithium containing compounds that can be accepted and released lithium ions instead of lithium metal. In 1979, novel rechargeable Li battery using lithium cobalt oxide ( $\text{LiCoO}_2$ ) as the positive electrode and lithium metal as the negative electrode were demonstrated by John Goodenough and Koichi Mizushima with voltage in the 4 V range.<sup>6</sup> In 1980, the reversible electrochemical intercalation of lithium in graphite that is the most currently used anode was first indicated by Rachid Yazami. Eventually, the first commercial LIBs using lithium cobalt oxide ( $\text{LiCoO}_2$ ) as the positive electrode and graphite as the negative electrode was manufactured by Sony and Asahi Kasei in 1991.<sup>7,8</sup>

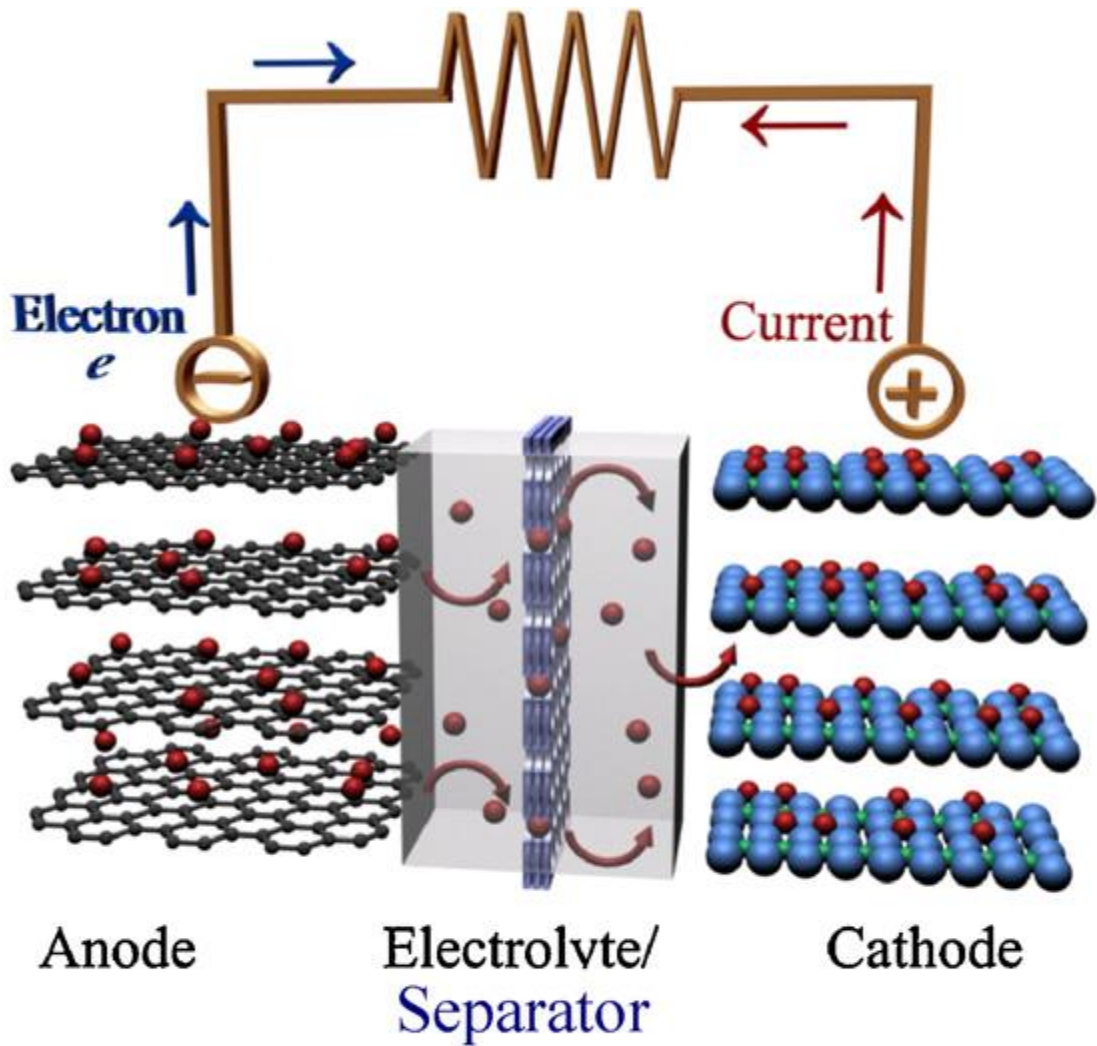


## 2.1. Basic Principles of Lithium-Ion Batteries

Lithium-ion batteries (LIBs) are composed of anode (e.g. carbonaceous (graphite, hard carbon, soft and carbon), metal (silicon, germanium, tin, antimony, and bismuth), metal oxide (tin oxide, copper oxide, iron oxide, ruthenium oxide, manganese oxide, and silicon oxide)), cathode (e.g. lithium manganese oxide (LiMnO<sub>2</sub>), lithium cobalt oxide (LiCoO<sub>2</sub>), and lithium iron phosphate (LiFePO<sub>4</sub>)), and Li salt containing electrolyte based on organic solvent, and separator (e.g. polyolefin). The components of LIBs will be explained concretely in next part. Commercial LIBs are mostly composed of graphite anode, LiCoO<sub>2</sub> cathode, LiPF<sub>6</sub> containing electrolyte, and polyolefin separator.<sup>9-11</sup>

LIBs are rechargeable batteries in which lithium ions move from negative electrode to the positive electrode during discharge and back when charging via the electrolyte, and electrons migrate via the outer electrical circuit as shown in Fig 1.2.1. The following equations demonstrate the chemical reactions during the discharge and charge at anode and cathode of commercial LIB. The cobalt electrode reaction is only reversible for  $x < 0.5$ , limiting the depth of discharge allowable.





- Carbon
- Li-ion
- Transition Metal
- Oxygen

**Figure 1.2.1.** Schematic of the principle of operation of commercial LIBs in which Li ions move from negative electrode to the positive electrode during discharge and back when charging.<sup>12</sup>

## 2.2. Components in Lithium-Ion Batteries

Lithium-ion batteries (LIBs) have four key components including cathode, anode, electrolyte, and separator as seen in Table 1.2.1.<sup>1, 13</sup> In case of cathodes, Li is located in lattice structure of cathode, while lithium escapes from the lattice as lithium ions during elimination. Therefore, structurally stable transition metal oxides have been used as cathode. In commercial LIBs, metal oxides or phosphate (e.g.  $\text{LiCoO}_2$ ,  $\text{LiMn}_2\text{O}_4$ ,  $\text{LiNiO}_2$ ,  $\text{LiFePO}_4$ , etc.) have been commonly used for the cathode materials.<sup>14</sup> However, these materials could not meet sufficient specific capacity and power density for large scale energy applications. In order to overcome these problems, various materials have been developed to increase specific capacity and power density by introducing novel materials such as  $\text{Li}(\text{Ni}_x\text{Mn}_y\text{Co}_{1-x-y})\text{O}_2$  type and  $\text{Li}_2\text{MnO}_3$ -stabilized  $\text{LiMo}_2$  ( $\text{M} = \text{Mn}, \text{Co}, \text{Ni}$ ), etc. In addition, owing to high cost of element in the cathode, development of cheaper cathode materials is inevitable (Figure 1.2.2).<sup>14</sup>

Since anode materials might stably store the released Li ions and supply the large electromotive force, they should have standard reduction potential similar to that of lithium. The most used anode in commercial LIBs is graphite.<sup>15, 16</sup> Nevertheless, the theoretical capacity of graphite anodes is  $372 \text{ mAh g}^{-1}$  which is insufficient for large scale energy applications. Therefore, lithium alloying compounds (e.g. Silicon (Si), Germanium (Ge), Antimony (Sb), Aluminum (Al), Tin (Sn), etc.)<sup>17-19</sup> and metal oxide having conversion reaction with lithium (e.g. Tin oxide, Copper oxide, Silicon monoxide, Silicon dioxide, etc.)<sup>20</sup> are considered to be to improve the specific capacity and energy density.

The electrolytes consist of lithium salt and non-aqueous organic solvent with electrochemical, thermal, and chemical stabilities in the range of working voltage.<sup>20</sup> Meanwhile, battery separator is a porous membrane that physically isolates a cathode and an anode and allows ionic transport via liquid electrolyte-filled pores during the passage of electric current. As the separator should prevent the short circuits caused by electrical contact between cathode and anode, separator is formed by polymer or ceramic materials that can be melted at high temperature. Moreover, the separators have poor wetting in electrolytes, low thermal and chemical stabilities. These demerits should be solved by introducing new materials or coating layers.<sup>21, 22</sup>

**Table 1.2.1.** Components and examples of materials of Lithium-Ion Batteries.

Component		Materials	Examples of Materials
	Cathode	Transition metal oxide	LiCoO <sub>2</sub> , LiMn <sub>2</sub> O <sub>4</sub> , LiNiO <sub>2</sub> , LiFePO <sub>4</sub>
	Anode	Carbon, Metal, Metal oxide	Graphite, Silicon, Germanium, Tin oxide, copper oxide, silicon oxide
	Separator	Polymer	Polyethylene (PE), polypropylene (PP), Polyvinylidene fluoride (PVdF)
	Lithium salt	Organic and inorganic lithium compound	LiPF <sub>6</sub> , LiBF <sub>4</sub> , LiAsF <sub>6</sub> , LiClO <sub>4</sub> , LiCF <sub>3</sub> SO <sub>3</sub> , Li(CF <sub>3</sub> SO <sub>2</sub> ) <sub>2</sub> N
Electrolyte	Electrolyte solvent	Nonaqueous organic solvent	Ethylene carbonate (EC), Propylene carbonate (PC), Dimethyl carbonate (DMC), Diethyl carbonate (DEC), Ethylmethyl carbonate (EMC)

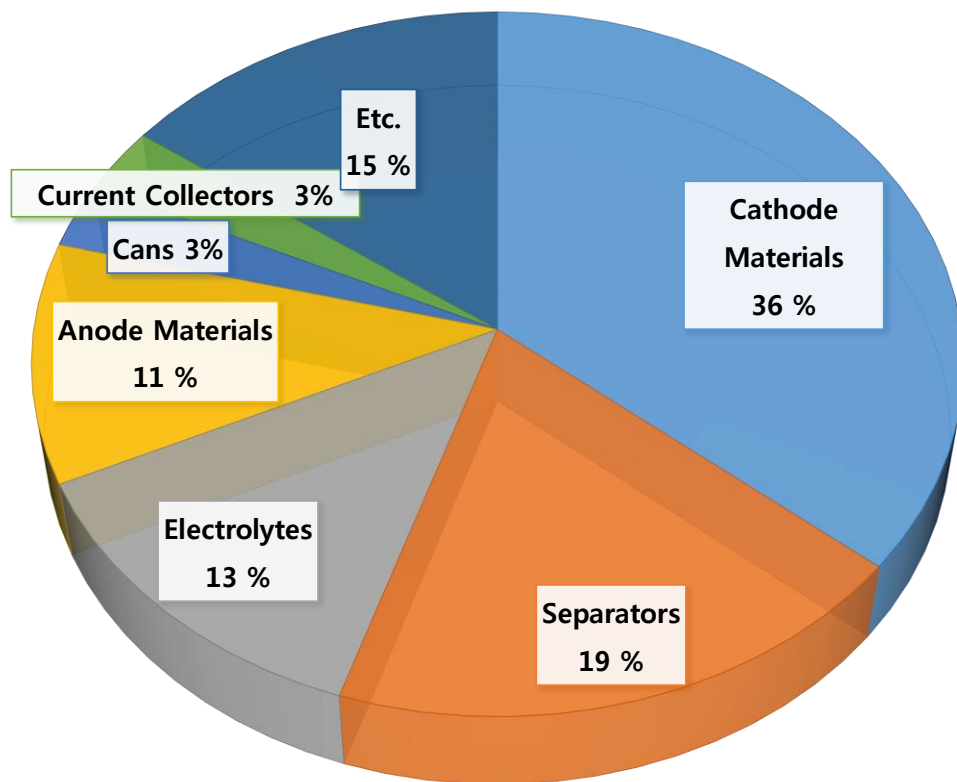


**Figure 1.2.2.** Cost Estimation of Lithium-Ion Batteries.

### 2.2.1. Cathode materials

Requirements of cathode materials are as follows: 1) A large amount of Li ions can be intercalated and deintercalated. In order to improve the energy efficiency during charging and discharging, they react reversibly and show constant flat voltage in wide range of composition. 2) It should be light and compact to have high specific energy and energy density, and have high electrical and ionic conductivity for high capacity. 3) It should exhibit long-term cycling stability. If the side reactions occur at positive or negative electrodes aside from flow of lithium ions, the efficiency is deteriorated. 4) As irreversible phase transition of crystal structure shortens the life of batteries, these phase transition should be prohibited during cycling. Furthermore, the capacity decreases as the active materials with large volume change detach from current collector. 5) It should be thermally, chemically, and electrochemically stable to avoid reaction with electrolyte. 6) Its particle should be spherical. In addition, distribution of particle size is narrow. These properties enhance the contact efficiency and electrical conductivity, and prevent to impair the aluminum foil (current collector) when making the electrodes.

The 3d transition metals are commonly used as cations of cathode materials. The 3d transition metals have a higher electrode potential, light weight, and small size than that of 4d and 5d transition metals. Therefore, they have advantageous to increase specific energy and energy density. The chalcogen group having structural stability are suitable for anions owing to repeated oxidation and reduction. Especially, oxygen is the most efficient element among chalcogens. During cycling, cations should be transferred quickly and easily when intercalating/deintercalating at cathode and anode and moving via electrolyte to have charge neutrality of transition metal oxides. In order to have reversibly broad potential range of oxidation/reduction within structure and minimize the change of crystal structure of active materials, the chosen cations should have lower charge number because they have small size and weak bonding with active materials. Although the ion radius of beryllium ions ( $\text{Be}^{2+}$ ) is smaller ( $0.45 \text{ \AA}$ ) than that of lithium ion ( $0.76 \text{ \AA}$ ) when having six coordination number, beryllium ion with large number of charge combines with oxygen strongly. Therefore, when  $\text{Be}^{2+}$  moves within crystal structure, they have repulsive power with other cations. While  $\text{Be}^{2+}$  is not suitable for cation as cathode, lithium ion can be used as cation due to their small size and low charge number. Lithium has advantage to increase the voltage of battery because the standard reduction potential of lithium is much lower ( $-3.040 \text{ V}$ ) than that of beryllium ( $-1.847 \text{ V}$ ).<sup>23</sup>

Typical lithium transition metal oxides for cathode materials can be classified according to their structures including: 1) layered structure ( $\text{LiMO}_2$ ,  $M = \text{Co, Mn, Ni}$ , and their combinations or substitutions), 2) spinel structure ( $\text{LiM}_2\text{O}_4$ ,  $M = \text{Co, Mn, Ni}$ ), and 3) polyanion structure ( $\text{Li}_x\text{M}_y(\text{XO}_4)_z$  ( $M = \text{metal, X} = \text{W, Mo, P, Si, etc.}$ )).<sup>10</sup> Table 1.2.2 demonstrates the electrochemical characteristics of

various types of cathode materials.<sup>14, 24-27</sup>

**Table 1.2.2.** Electrochemical Characteristics of Various types of Cathode materials.

Compounds	Theoretical capacity (mAh g <sup>-1</sup> )	*Practical capacity (mAh g <sup>-1</sup> )	Average voltage (V vs. Li/Li <sup>+</sup> )	Tap density (g/cc)
LiCoO <sub>2</sub>	274	~150	3.9	5.1
LiNiO <sub>2</sub>	275	215	3.7	4.7
LiNi <sub>1-x</sub> Co <sub>x</sub> O <sub>2</sub> (0.2 ≤ x ≤ 0.5)	~280	~180	3.8	4.8
LiNi <sub>1/3</sub> Mn <sub>1/3</sub> Co <sub>1/3</sub> O <sub>2</sub>	278	~154	3.7	4.8
LiNi <sub>0.5</sub> Mn <sub>0.5</sub> O <sub>2</sub>	280	130 - 140	3.8	4.6
LiMnO <sub>2</sub>	148	~130	4.0	4.2
LiNi <sub>2-x</sub> M <sub>x</sub> O <sub>4</sub> (M = Al, Li, etc.)	148	~100	4.0	4.2
LiFePO <sub>4</sub>	170	~160	3.4	3.6

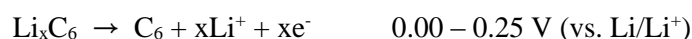
\* Practical capacity: Commercially available capacity.



### 2.2.2. Anode materials

In rechargeable lithium-ion batteries, spontaneous oxidation reactions occur at anode materials during discharge, while spontaneous reduction reactions happen at cathode materials. For example, in lithium-ion battery consisting of  $\text{Li}_x\text{C}/\text{Li}_{1-x}\text{CoO}_2$ , the anode active material,  $\text{Li}_x\text{C}$ , donates electrons and lithium ions during discharge. In this case,  $\text{Li}_x\text{C}$  itself oxidizes. Simultaneously, the cathode active material,  $\text{Li}_{1-x}\text{CoO}_2$ , accepts electrons and lithium ions. In this case,  $\text{Li}_{1-x}\text{CoO}_2$  itself reduces. Consequentially, anode stores and releases lithium ions during charge and discharge, respectively.<sup>28-30</sup>

In the case of graphite anode, one lithium ion reacts theoretically with six carbons, as shown in the following equation. The voltage of the graphite anode in comparison with the lithium electrode ( $\text{Li}/\text{Li}^+$ ) ranges from 0.0 to 0.25 V and its theoretical capacity is  $372 \text{ mAh g}^{-1}$ . Though the potential of pristine graphite is about 3.0 V, it starts to decline rapidly when lithium is intercalated. For both the cathode and anode materials, the potential of the lithium electrode decreases by increasing lithium within the electrode active material, finally reaching 0 V.<sup>28-30</sup>



Decomposition of the electrolyte takes place at the surface of the anode during charging as its reduction potential is relatively higher than that of lithium. These decomposition causes the formation of solid electrolyte interphase (SEI) at the surface of the electrode. SEI layer suppresses the electron transfer reactions between the anode and the electrolyte, thus preventing further electrolyte decomposition. The performance of LIBs is strongly influenced by the characteristics of the SEI layer deposited at the electrode surface. Numerous researches are being made to produce a more compact SEI film with outstanding electrochemical properties by introducing additives that induce decomposition prior to the electrolyte decomposition.<sup>31</sup>

The performance of LIBs including energy density, power density, and cycle life is affected by anode materials. In order to maximize the performance of lithium secondary batteries, anode active materials should fulfill the following conditions: 1) Anode materials should have a low reaction potential corresponding to a standard electrode and provide a high cell voltage with the cathode. The potential relating to electrochemical reactions must be a close approximation of the electrochemical potential of lithium metal. 2) The change of structure should be minimized during reaction with lithium ions. In the case of existing the change of structure, the crystal strain accumulates and it hinders the reversibility of electrochemical reactions, thus resulting in poor cycle performance. 3) It should engage in highly reversible reactions with lithium ions. Ideal reversible reactions have 100 % charge/discharge efficiency, indicating no change in reaction efficiency with cycles. 4) The speed of diffusion should be

fast within anode active materials. Especially, the speed of diffusion relatively plays an important role to realize cell performance. 5) High electronic conductivity is necessary to facilitate the movement of electrons during electrochemical reactions. 6) The density of anode active materials should be high in dense to obtain the high electrode density. This is an important design factor that is considered to enhance battery energy. For instance, graphite material shows a theoretical density of 2.2 g/cc and a theoretical capacity density of 818 mAh/cc. 7) It should store a large amount of charge (coulomb) per unit mass.

Other important factors that determine energy density and power density are specific surface area, tap density, particle size, and distribution. Since the anode has a large specific capacity per unit mass, it is more difficult to intercalate or deintercalate lithium ions in comparison with the cathode. Therefore, the design of the anode should take into account the fast movement of lithium ions to improve the performance of LIBs. Table 1.2.3 shows the main characteristics of common anode active materials.<sup>32</sup>

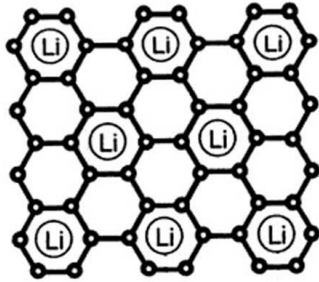
Typical anode materials can be classified according to their reaction with lithium ions as follows (Fig 1.2.3): 1) Formation of lithium-graphite intercalation compounds (carbon based anode materials; graphite, amorphous carbon, hard/soft carbon, etc.)<sup>15, 16</sup> 2) Formation of metal alloy (group IV elements; silicon, tin, germanium, aluminum, and antimony, etc.),<sup>17-19</sup> and 3) Conversion reaction with lithium (transition metal oxides; Fe<sub>2</sub>O<sub>3</sub>, Fe<sub>3</sub>O<sub>4</sub>, CuO, Cu<sub>2</sub>O, NiO, Ni<sub>2</sub>O, MnO, MnO<sub>2</sub>, etc.)<sup>20</sup>

**Table 1.2.3.** Main characteristics of common anode active materials.

<b>Material</b>	<b>Theoretical capacity (mAh g<sup>-1</sup>)</b>	<b>*Practical capacity (mAh g<sup>-1</sup>)</b>	<b>Average voltage (V)</b>	<b>Tap density (g/cc)</b>
Lithium metal	3800	-	0.0	0.535
Graphite	372	~360	~0.1	2.2
Cokes	-	~170	~0.15	<2.2
Silicon	4200	~1000	~0.16	2.36
Tin	790	~700	~0.4	7.30

\* Practical capacity: Commercially available capacity.

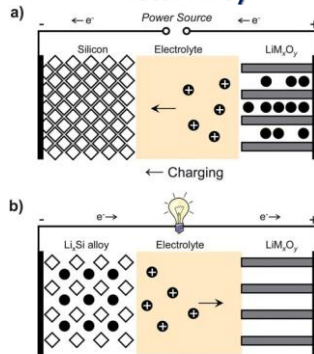
**Carbon- base (Intercalation)**



*J. Power Sources* **2012**, *208*, 74-85.

- Graphite
- Graphitized material  
(e.g. Artificial carbon,  
amorphous carbon)
- Hard/soft carbon  
 $\text{Li}_x\text{C}_6 \leftrightarrow \text{C}_6 + x\text{Li}^+ + xe^-$

**Metal-Alloy**



*Energy Environ. Sci.* **2011**, *4* (1), 56-72.

- Group IV elements
  - Silicon (Si)
  - Tin (Sn)
  - Germanium (Ge)
- $$\text{Li}_{4.4} + \text{Si} \leftrightarrow \text{Li}_{4.4}\text{Si}$$

**Metal oxide  
(Conversion)**



- Tin oxide ( $\text{SnO}_2$ )
  - Copper oxide ( $\text{CuO}$ )
  - Silicon monoxide ( $\text{SiO}$ )
  - Silicon dioxide ( $\text{SiO}_2$ )
- $$\text{M}_x\text{O}_y + \text{ALi}^+ + \text{Ae}^- \leftrightarrow \text{ALi}_2\text{O} + x\text{M}$$

**Figure 1.2.3.** The three types of Anode Materials for LIBs.<sup>33</sup>

### 2.2.3. Separators

A Separator is one of the key components of LIBs as important materials that physically isolate a cathode and an anode and allow ionic transport via liquid electrolyte-filled pores during the passage of electric current even if the separator itself doesn't participate in electrochemical reaction.

The separator for lithium secondary batteries is fine porous polymer film. The most conventional separator is polyolefin with semi crystalline structure such as polyethylene (PE) and polypropylene (PP). The merits of polyolefin are excellent mechanical strength, chemical stability, and inexpensive price. Commercial separators have usually 0.3 – 1  $\mu\text{m}$  sized pore, porosity of 30 – 50 %, and low thermal shutdown temperature (PE:  $\sim 135$   $^{\circ}\text{C}$ , PP:  $\sim 165$   $^{\circ}\text{C}$ ).

Several requirements of the separators for LIBs should be satisfied. Table 1.2.4 shows requirements for separator of LIBs. Generally, separator has a thickness of  $\sim 20$   $\mu\text{m}$ , pore size of under 1  $\mu\text{m}$ , and porosity of 40% that can be passed through lithium ions and prevented dendritic lithium penetration. Also, it is desirable that the separator has low electrical resistance when it is wet with electrolyte. The cell performance such as discharge capacity deteriorates with high electrical resistance. Batteries require the separator having good wettability with electrolyte. At high temperature, separator is critical component to influence on chemical and thermal stability in battery under oxidation/reduction conditions. Also, separators play an important role in safety. When the temperature inside battery increase rapidly by internal short circuit, the separator is melted, prevents to move the lithium ions, impedes the exothermic reaction, and enhances safety of batteries.<sup>34</sup>

Separator materials have been studied by using polyolefin microporous films (PE, PP), polyvinylidene fluoride (PVdF)<sup>22</sup>, inorganic nanoparticle ( $\text{SiO}_2$ ,  $\text{TiO}_2$ ,  $\text{Al}_2\text{O}_3$ ,  $\text{ZrO}_2$ , etc.) coated polymer.<sup>35</sup>

**Table 1.2.4.** Requirements for Separators.<sup>24</sup>

<b>Parameter</b>	<b>Specification</b>
Thickness	< 25 $\mu\text{m}$
Electrical resistance	< 2 Ohms $\text{cm}^2$
Pore size	< 1 $\mu\text{m}$
Porosity	~ 40 %
Mix penetration strength	> 100 kgf/mil
Shrinkage	< 5 % in both MD and TD
Shut down temperature	~ 130 $^{\circ}\text{C}$
High-temp melt integrity	> 150 $^{\circ}\text{C}$
Wettability	Complete wet out in typical battery electrolytes
Chemical Stability	Stable in battery for long period of time

#### 2.2.4. Electrolytes

Electrolytes can be considered as an intermediate allowing a transport of lithium ion. Roles of electrolytes are dissociation of lithium salts, transportation of solvated lithium ions between cathode and anode, and effective electrochemical reaction at the interface. Typically, electrolytes consist of solvent and lithium salt. In case of liquid solvent or solid such as inorganic compounds or polymer, it is called liquid electrolyte or solid electrolyte, respectively. LIBs commonly use materials that can insert/extract the lithium ions as the cathode and anode, and are injected with liquid electrolyte between electrodes. The electrolyte transfers of lithium ions from cathode to anode during charging and vice versa.<sup>36</sup>

The electrolyte for lithium secondary batteries is used organic solution mixed lithium salt and organic solvent. Though there are many kinds of organic solvent and lithium salt, usable electrolyte in LIBs is limited. As LIBs operate at high voltage, the organic solvent is necessarily used. The organic solvent has lower dielectric constant than that of aqueous solvent. Dielectric constant affects lithium dissociation. If solvent has higher dielectric constant, lithium dissociation becomes easier. However, a high dielectric constant results in a high viscosity, leading to decrease of ionic conductivity. Therefore, electrolytes consists of co-solvent, which is mixed with a low viscosity solvent and a high permittivity solvent, and a lithium salt prepared by dissolving a predetermined concentration.<sup>37</sup>

In order to apply to LIBs, the following properties are requirements of lithium salts: intrinsic thermal stability, high oxidation limit of the anion (electrochemical stability), low reduction limit of the anion, good solubility of the salt in appropriate solvents, chemical stability with the solvent, high conductivity of its solutions, low molecular weight, and low cost. When considered overall conditions, lithium hexafluorophosphate ( $\text{LiPF}_6$ ) is generally used as lithium salt due to high ionic conductivity and good electrochemical stability.<sup>37</sup>

### 2.3. References

1. H. K. Bruce Dunn, Jean-Marie Tarascon, Electrical energy storage for the grid: a battery of choices. *Science* **2011**, *334* (6058), 928-935.
2. H. Chen, T. N. Cong, W. Yang, C. Tan, Y. Li and Y. Ding, Progress in electrical energy storage system: A critical review. *Progress in Natural Science* **2009**, *19* (3), 291-312.
3. M. M. Farid, A. M. Khudhair, S. A. K. Razack and S. Al-Hallaj, A review on phase change energy storage: materials and applications. *Energy Convers. Manage.* **2004**, *45* (9-10), 1597-1615.
4. J.-M. T. a. M. Armand, Issues and challenges facing rechargeable lithium batteries. *Nature* **2001**, *414* (6861), 359-367.
5. M. S. Whittingham, Electrical energy storage and intercalation chemistry. *Science* **1976**, *192* (4244), 1126-1127.
6. A. Yoshino, The birth of the lithium-ion battery. *Angew. Chem. Int. Ed. Engl.* **2012**, *51* (24), 5798-5800.
7. N. S. Choi, Z. Chen, S. A. Freunberger, X. Ji, Y. K. Sun, K. Amine, G. Yushin, L. F. Nazar, J. Cho and P. G. Bruce, Challenges facing lithium batteries and electrical double-layer capacitors. *Angew. Chem. Int. Ed. Engl.* **2012**, *51* (40), 9994-10024.
8. M. R. Palacin, Recent advances in rechargeable battery materials: a chemist's perspective. *Chem. Soc. Rev.* **2009**, *38* (9), 2565-2575.
9. M. Winter, and Ralph J. Brodd, What are batteries, fuel cells, and supercapacitors? *Chem. Rev.* **2004**, *104* (10), 4245-4270.
10. Z. Gong and Y. Yang, Recent advances in the research of polyanion-type cathode materials for Li-ion batteries. *Energy Environ. Sci.* **2011**, *4* (9), 3223.
11. V. Etacheri, R. Marom, R. Elazari, G. Salitra and D. Aurbach, Challenges in the development of advanced Li-ion batteries: a review. *Energy Environ. Sci.* **2011**, *4* (9), 3243.
12. M.-K. Song, S. Park, F. M. Alamgir, J. Cho and M. Liu, Nanostructured electrodes for lithium-ion and lithium-air batteries: the latest developments, challenges, and perspectives. *Materials Science and Engineering: R: Reports* **2011**, *72* (11), 203-252.
13. P. B. ANTONINO SALVATORE ARICÒ, BRUNO SCROSATI, JEAN-MARIE ARASCON AND WALTER VAN SCHALKWIJK, Nanostructured materials for advanced energy conversion and storage devices. *Nat. Mater.* **2005**, *4* (5), 366-377.
14. M. S. Islam and C. A. Fisher, Lithium and sodium battery cathode materials: computational insights into voltage, diffusion and nanostructural properties. *Chem. Soc. Rev.* **2014**, *43* (1), 185-204.



15. C. de las Casas and W. Li, A review of application of carbon nanotubes for lithium ion battery anode material. *J. Power Sources* **2012**, *208*, 74-85.
16. Y. P. Wu, E. Rahm and R. Holze, Carbon anode materials for lithium ion batteries. *J. Power Sources* **2003**, *114* (2), 228-236.
17. C. M. Park, J. H. Kim, H. Kim and H. J. Sohn, Li-alloy based anode materials for Li secondary batteries. *Chem. Soc. Rev.* **2010**, *39* (8), 3115-3141.
18. W.-J. Zhang, A review of the electrochemical performance of alloy anodes for lithium-ion batteries. *J. Power Sources* **2011**, *196* (1), 13-24.
19. J. R. Szczech and S. Jin, Nanostructured silicon for high capacity lithium battery anodes. *Energy Environ. Sci.* **2011**, *4* (1), 56-72.
20. B. Scrosati, Recent advances in lithium ion battery materials. *Electrochim. Acta* **2000**, *45* (15), 2461-2466.
21. F. Croce, M. L. Focarete, J. Hassoun, I. Meschini and B. Scrosati, A safe, high-rate and high-energy polymer lithium-ion battery based on gelled membranes prepared by electrospinning. *Energy Environ. Sci.* **2011**, *4* (3), 921.
22. C. M. Costa, M. M. Silva and S. Lanceros-Méndez, Battery separators based on vinylidene fluoride (VDF) polymers and copolymers for lithium ion battery applications. *RSC Adv.* **2013**, *3* (29), 11404.
23. J. B. Goodenough and Y. Kim, Challenges for Rechargeable Li Batteries†. *Chem. Mater.* **2010**, *22* (3), 587-603.
24. B. Xu, D. Qian, Z. Wang and Y. S. Meng, Recent progress in cathode materials research for advanced lithium ion batteries. *Materials Science and Engineering: R: Reports* **2012**, *73* (5-6), 51-65.
25. T. Aoshima, Okahara, K., Kiyohara, C., & Shizuka, K, Mechanisms of manganese spinels dissolution and capacity fade at high temperature. *J. Power Sources* **2001**, *97*, 377-380.
26. M. S. Whittingham, Lithium Batteries and Cathode Materials. *Chem. Rev.* **2004**, *104* (10), 4271-4302.
27. J. W. Fergus, Recent developments in cathode materials for lithium ion batteries. *J. Power Sources* **2010**, *195* (4), 939-954.
28. M. B. R.Tossici, V. Nalimova,a and R. Marassi, A High-Rate Carbon Electrode for Rechargeable Lithium-Ion Batteries. *J. Electrochem. Soc.* **1996**, *143* (3), L64-L67.
29. B. S. S. Flandrois, Carbon materials for lithium-ion rechargeable batteries. *Carbon* **1999**, *37* (2), 165-180.
30. M. Yoshio, H. Wang and K. Fukuda, Spherical Carbon-Coated Natural Graphite as a Lithium-Ion Battery-Anode Material. *Angew. Chem.* **2003**, *115* (35), 4335-4338.

31. B. V. Ratnakumar, M. C. Smart, and S. Surampudi, Effects of SEI on the kinetics of lithium intercalation. *J. Power Sources* **2001**, *97*, 137-139.
32. Y. Xie and C. Wu, Design of nanoarchitected electrode materials applied in new-generation rechargeable lithium ion batteries. *Dalton Trans.* **2007**, DOI: 10.1039/b712525a (45), 5235.
33. S. Goriparti, E. Miele, F. De Angelis, E. Di Fabrizio, R. Proietti Zaccaria and C. Capiglia, Review on recent progress of nanostructured anode materials for Li-ion batteries. *J. Power Sources* **2014**, *257*, 421-443.
34. X. Huang, Separator technologies for lithium-ion batteries. *J. Solid State Electrochem.* **2010**, *15* (4), 649-662.
35. S. M. Kang, M.-H. Ryou, J. W. Choi and H. Lee, Mussel- and Diatom-Inspired Silica Coating on Separators Yields Improved Power and Safety in Li-Ion Batteries. *Chem. Mater.* **2012**, *24* (17), 3481-3485.
36. K. Xu, Nonaqueous liquid electrolytes for lithium-based rechargeable batteries. *Chem. Rev.* **2004**, *104* (10), 4303-4418.
37. S. S. Zhang, A review on electrolyte additives for lithium-ion batteries. *J. Power Sources* **2006**, *162* (2), 1379-1394.

## Chapter II. Multifunctional Natural Polysaccharide Binder for Lithium-Ion Battery Anodes

### 1. Introduction

Lithium-ion batteries (LIBs) have several advantages such as light weight, high working voltage (3.6 V), high energy density, long cycle life and no memory effect, compared to conventional nickel-cadmium and lead-acid batteries.<sup>1-3</sup> Owing to these properties, LIBs have been widely used for portable electronic devices including mobile phones, laptops, tablets, and digital cameras. However, hybrid electric vehicles (HEVs), plug-in hybrid electric vehicles (PHEVs), electric vehicles (EVs), and energy storage systems (ESS) require higher energy density and higher power density than those of conventional LIBs consisting of LiCoO<sub>2</sub> cathode and graphite anode. Therefore, the development of alternative materials having higher specific capacity is inevitable.<sup>4-6</sup>

Silicon (Si) has attracted much attention as promising anode material due to its high theoretical capacity (3579 mA h g<sup>-1</sup> with composition of Li<sub>15</sub>Si<sub>4</sub> at room temperature), relatively low working potential (< 0.4 versus Li/Li<sup>+</sup>), its abundance in nature, and low cost.<sup>7-10</sup> However, the large volume change of Si (> 300% with composition of Li<sub>3.75</sub>Si at room temperature) during lithiation/delithiation leads to a serious aggregation of Si, the formation of unstable thick solid-electrolyte-interface (SEI) layers and depletion of electrolyte, which will make critical capacity fading. Furthermore, Si has low electrical conductivity and sluggish lithium-ion diffusivity. These fatal flaws prevent the commercialization of Si anode.<sup>11-13</sup>

There are several solutions to overcome these drawbacks, including Si composites with metal oxide, inactive metals, or carbon materials<sup>14-17</sup> and Si nanostructuring (e.g., nanoparticles,<sup>18</sup> nanowires,<sup>19</sup> and nanotubes).<sup>20</sup> Especially, Si/C composites showed long cycle life, and great rate performance because high electrical conductivity of carbon compensated drawback of Si.<sup>14, 16, 17</sup> Another attempt has been tried to develop functional polymeric binders which can alleviate severe volume change of Si anodes. Actually, overall quality of batteries depends on performance of binders, because polymeric binders give adhesion between electrode and current collector, allowing long-term cycling stability. Until now, the most conventional binder, polyvinylidene fluoride (PVdF), has been used for carbonaceous anodes and cathode materials with low volume change during cycling. However, since Si suffers from a serious volume expansion (> 300%) during cycling, PVdF binders with tensile strength of ~22 MPa cannot interrupt the pulverization of Si electrodes.<sup>21-23</sup> Therefore, carboxymethyl cellulose (CMC),<sup>21</sup> poly(acrylic acid) (PAA),<sup>24</sup> polyamide imide (PAI),<sup>23</sup> alginate extracted from brown algae,<sup>25</sup> NaOH-neutralized poly(acrylic acid),<sup>26</sup> PAA/CMC,<sup>27</sup> agarose/PAA,<sup>28</sup> and hyperbranched β-cyclodextrin polymer<sup>29</sup> were developed as alternative binders for Si anode. In addition, there were novel binders for LiMn<sub>2</sub>O<sub>4</sub> (LMO) cathode such as poly(acrylonitrile-methyl methacrylate)<sup>30</sup>, PAA, polyvinyl

alcohol (PVA), polyacrylonitrile (PAN), PVdF,<sup>31</sup> alginate extracted from brown seaweed,<sup>32</sup> and lithiated perfluorosulfonate ionomer.<sup>33</sup> PAN provides appropriate amount of electrolyte uptake and low impedance.<sup>31</sup> Alginate binder resolved  $Mn^{2+}$  dissolution, which showed applicable possibility for commercial LIBs employing LMO electrodes.<sup>32</sup> Lithiated perfluorosulfonate ionomer has lower interface resistance, and thus leads to higher capacity and enhanced cycling stability even under harsh conditions (high rate (5-20 C) and at high temperature of 60 °C).<sup>33</sup>

Herein, we demonstrate natural polysaccharide binder for Si-based anode and Si/C composite materials and  $LiMn_2O_4$  cathodes. The introduction of agarose binder containing many functional groups to nanostructured Si foam anodes provides a strong adhesion between Si foam and current collector, leading to enhanced electrochemical properties, including a high specific capacity of 1028 mAh g<sup>-1</sup> (60% retention compared to 2<sup>nd</sup> cycle) and outstanding cycling performance after 200 cycles. Si/C composite (Si foam@HC@C made by carbonization of Si-dispersed agarose) electrode showed first discharge capacity and discharge capacity were 654 and 513 mAh g<sup>-1</sup> with enhanced initial coulombic efficiency of 78.4%, compared to HC@C with initial coulombic efficiency of 71.6%.  $LiMn_2O_4$  cathode with agarose binder exhibited high initial coulombic efficiency of 96.2% and stable cycling performance with nearly 100% coulombic efficiency.

## 2. Experimental

### 2.1 Synthesis of Si foam @ Hard Carbon (HC) @ C

**Preparation of nanostructured Si foam:** 10.0 g Al-Si alloy powder (325 mesh, 99%, Al:Si = 88:12 wt.%, Alfa Aesar) was immersed in 400 mL of 3 M hydrochloric acid (HCl) solution (SAMCHUN chemical, Korea) for 60 min with stirring. The chemically etched powder was filtered, washed several times with deionized (DI) water and dried at 70 °C for 12 hr. At this condition, we obtained the production yield of 11%.

**Preparation of HC@C:** 2.0 g of agarose (from Sigma-Aldrich) was dissolved into 60ml of deionized (DI) water with stirring at 95 °C for 1 hr. The solution became transparent and then it was moved to a glass container for gelation at room temperature for 1 h. The resultant product was dried at 70 °C in a convection oven for 12 h. Subsequently, carbonization process of the agarose was conducted in a quartz tube furnace and ramping rate is 5 °C min<sup>-1</sup>. The dried agarose film was heated to 500 °C for 1 h under argon atmosphere for stabilization and increased to 900 °C for 2h to enhance electrical conductivity and to increase the carbon quality. As synthesized HC particles were heated to 900 °C at a ramping rate of 10 °C min<sup>-1</sup> in a quartz tube furnace under argon atmosphere. After temperature reached to 900 °C, we switched the gas in the tube furnace with acetylene gas (10% diluted in argon) and carbon coated on the surface of HC for 2 min with 500 cc min<sup>-1</sup>.

**Synthesis of Si foam@HC@C:** 0.07 g of Si foam was dispersed in 25mL of dimethyl sulfoxide (DMSO) with stirring and sonication at room temperature for 60 min. 2.16 g of agarose (from Sigma-Aldrich) was added into Si foam solution with stirring at 70 °C for 1 day. Then it was moved to a glass petri dish for evaporation of solvent at 150 °C for 1 day. Subsequently, carbonization process was identical with that of HC. In order to make stable SEI layer and increase electrical conductivity of Si foam@HC, carbon coating was conducted using acetylene gas. Si foam@HC was carbon coated in the same way of HC.

### 2.2 Characterization

Scanning electron microscopy (SEM, S-4800, Hitachi) at an accelerating voltage of 10kV was used to characterize morphologies of Si foam and Si foam@HC@C samples. To investigate the microstructures of samples, X-ray diffractometer (XRD, D8 Advance, Bruker, Cu K $\alpha$  radiation) was used between 10 and 90° at a scan rate of 1.4° sec<sup>-1</sup>. The nitrogen adsorption and desorption isotherms were measured with a VELSORP-mini II (BEL Japan, Inc.) at 77 K in the relative pressure range of P/P<sub>0</sub> from 0.05 to 0.3 to examine the BET surface areas and pore size distribution. Total reflectance–Fourier transform infrared (ATR-FTIR) spectra of electrodes were recorded in reflectance measurements using a Varian 670-IR spectrometer with a spectral resolution of 4 cm<sup>-1</sup> under a nitrogen

atmosphere. The stress-strain curves of the agarose and PVdF film were measured using a universal testing machine (AGS-100NX, SHIMADZU). Thermogravimetric analyzer (TGA, TA Instruments, USA) was used to measure the amount of carbon between 40 and 700 °C at a ramping rate of 5 °C min<sup>-1</sup> under air atmosphere at a scan rate of 5 °C min<sup>-1</sup>.

### 2.3 Electrochemical measurements

For the electrochemical measurements of Si foam, the anode was prepared by mixing 60 wt% active material (etched Al-Si powder), 20 wt% of super P and 20 wt% of binder (5 wt% of agarose (Aldrich) in dimethyl sulfoxide (DMSO)) with a mixer (Thinky mixer, ARE310) at 2200 rpm for 15 min to homogenize slurry. Another anode (HC@C and Si foam@HC@C) were composed of active materials, super P, agarose binder at a weight ratio of 80:10:10. The cathode (LiMn<sub>2</sub>O<sub>4</sub>) was made of 80 wt% of active material (LiMn<sub>2</sub>O<sub>4</sub>), 10 wt% super P, and 10 wt % of binder (5 wt% of agarose in DMSO). After the slurries were casted on a copper/aluminium foil, the electrodes were dried at 150 °C for 12 hr in a vacuum oven to solidify electrodes and evaporate DMSO. The mass loading level of Si foam, Si foam@HC@C, HC@C, and LiMn<sub>2</sub>O<sub>4</sub> in electrodes was around 0.8, 1.9, 2.2, and 2.3 mg cm<sup>-2</sup>. The coin-type half-cell (2016R) was assembled in an Ar-filled glove box with oxygen and water less than 1 ppm. The Li metal foil was used as counter electrode and micro porous polyethylene film (Celgard 2400) was used as a separator. The electrolyte consisted of a solution of 1.3M LiPF<sub>6</sub> in a mixture of ethylene carbonate (EC)/diethyl carbonate (DEC) (3:7, v/v) with 10% fluorinated ethylene carbonate (FEC) additive in Si foam/Li, Si foam@HC@C/Li, HC@C/Li half-cell. In LiMn<sub>2</sub>O<sub>4</sub>/Li half-cell, the electrolyte consisted of 1M LiPF<sub>6</sub> in a mixture of ethylene carbonate (EC)/dimethyl carbonate (DMC) (3:7, v/v). Galvanostatic charge and discharge cycling (WonATech WBCS 3000 battery measurement system) was performed at 25 °C.

### 3. Results and discussion

#### 3.1. Preparation of nanostructured Si foam and its electrochemical test using agarose binder

Nanostructured Si foam was prepared via a simple chemical etching of Al-Si alloy powder by using acid solution, as seen in Figure 2.1(a) and (b). Pristine Al-Si powder with 1-6  $\mu\text{m}$  in size and spherical shape was immersed into 3M hydrochloric acid (HCl) solution with a mild stirring at room temperature for 1 h. After the chemical etching process, although the etched Al-Si powders have foam-like structure with a thin Si frame, the particles were seriously etched away with a destruction of the original structure. Transmission electron microscopy (TEM) image (Figure 2.1(b), inset) shows porous structure of Si foam with frame in range of 50-100 nm. Pristine Al-Si powder (Figure 2.1(c)) and the chemically etched Al-Si particles (Figure 2.1(d)) were investigated by X-ray diffraction (XRD) patterns in order to confirm the existence of aluminum. After the chemical etching, Al peaks completely disappeared, while only Si peaks were left over, indicating the complete dissolution of Al (Figure 2.1(d)). In order to determine the porosity of Si foam, nitrogen adsorption-desorption measurements were conducted (Figure 2.1(e)). The specific surface area of Si foam calculated with the Brunauer-Emmett-Teller (BET) equation is  $80.8 \text{ m}^2 \text{ g}^{-1}$ . As shown in Figure 2.1(f), the pore size distribution (PSD) curve of Si foam was retrieved with the Barrett-Joyner-Halenda (BJH) model by using the adsorption branch and suggests Si foam has many nanopores. High specific surface area and numerous nanopores provide a large interfacial area between the electrolyte and the active materials. Probably, it results in enhancement of electrochemical performance by controlling a large volume change of Si anodes. Nevertheless, nanostructuring cannot become perfect alternative to restrain the severe volume expansion of Si. In order to resolve this problem, many researchers have usually introduced new binder material to improve cycle retention. In this study, natural polysaccharide, agarose, was used as polymeric binder for Si foam anodes, because agarose contains many functional groups, including ether (R-O-R) and hydroxyl group (R-OH), which are expected to generate strong adhesion between agarose and surface of Si. Simple peel-off test was carried out on agarose and polyvinylidene fluoride (PVdF) coated Si wafer (Figure 2.2). Agarose and PVdF binders were spin-coated on Si wafer by spinning at 2000 rpm for 2 min, and subsequently dried at 150  $^{\circ}\text{C}$  for 12 h. When they took polymer films off using 3M scotch tape, agarose coated Si wafer did not change, while PVdF coating layer on Si wafer was completely peeled off due to the weak adhesion between PVdF and surface of Si wafer. To investigate the adhesion of agarose on the Si surface, Fourier transform infrared (FTIR) spectroscopy was used for agarose film, Si foam powder, and electrode consisted of Si foam and agarose (Figure 2.3(a)). Agarose film has a broad peak at  $\sim 3420 \text{ cm}^{-1}$  assigned to hydroxyl group related to hydrogen-bonded O-H stretching vibrations, peak at  $1647 \text{ cm}^{-1}$  related to C=O stretch, and peak at  $1070 \text{ cm}^{-1}$  related to C-O-C

asymmetric vibrations. The spectrum of electrode supports for strong adhesion between Si foam and agarose as an obvious peak at  $\sim 1036\text{ cm}^{-1}$  demonstrates Si-O-Si band. The intensity of peak appearing at  $\sim 3420\text{ cm}^{-1}$  (assigned to hydroxyl group) decreases after the formation of electrode, indicating the strong interactions between agarose and the Si surface. Also, Figure 2.3(b) shows that agarose film has higher stiffness than PVdF film. These properties will affect the cycling properties of Si-based electrode.

Electrochemical performance of Si foam was tested as shown in Figure 2.4. Si foam electrodes with agarose and PVdF binder were tested in the potential range of 0.005-1.5 V (versus Li/Li<sup>+</sup>) in a coin-type half cell (2016R). Figure 2.4(a) shows the first cycle voltage profiles of Si electrodes obtained at the C/20 rate. The electrodes using agarose and PVdF binder showed the charge capacity of 2172 and 658 mAh g<sup>-1</sup> and the initial coulombic efficiency of 82.6% and 25.8%, respectively. Agarose binder suppresses the detachment and loss of Si from current collector, while the PVdF binder cannot grasp the Si foam during lithiation, resulting in detachment between active material and current collector. Moreover, cycle retention of the cell using agarose and PVdF binder was different, which Si foam electrode with agarose binder exhibited 1028 mAh g<sup>-1</sup> after 200 cycles (capacity retention of 60% compared to 2<sup>nd</sup> cycle). However, the cell with PVdF binder showed a fast capacity decay due to the poor adhesion between PVdF binder and Si foam after first few cycles.



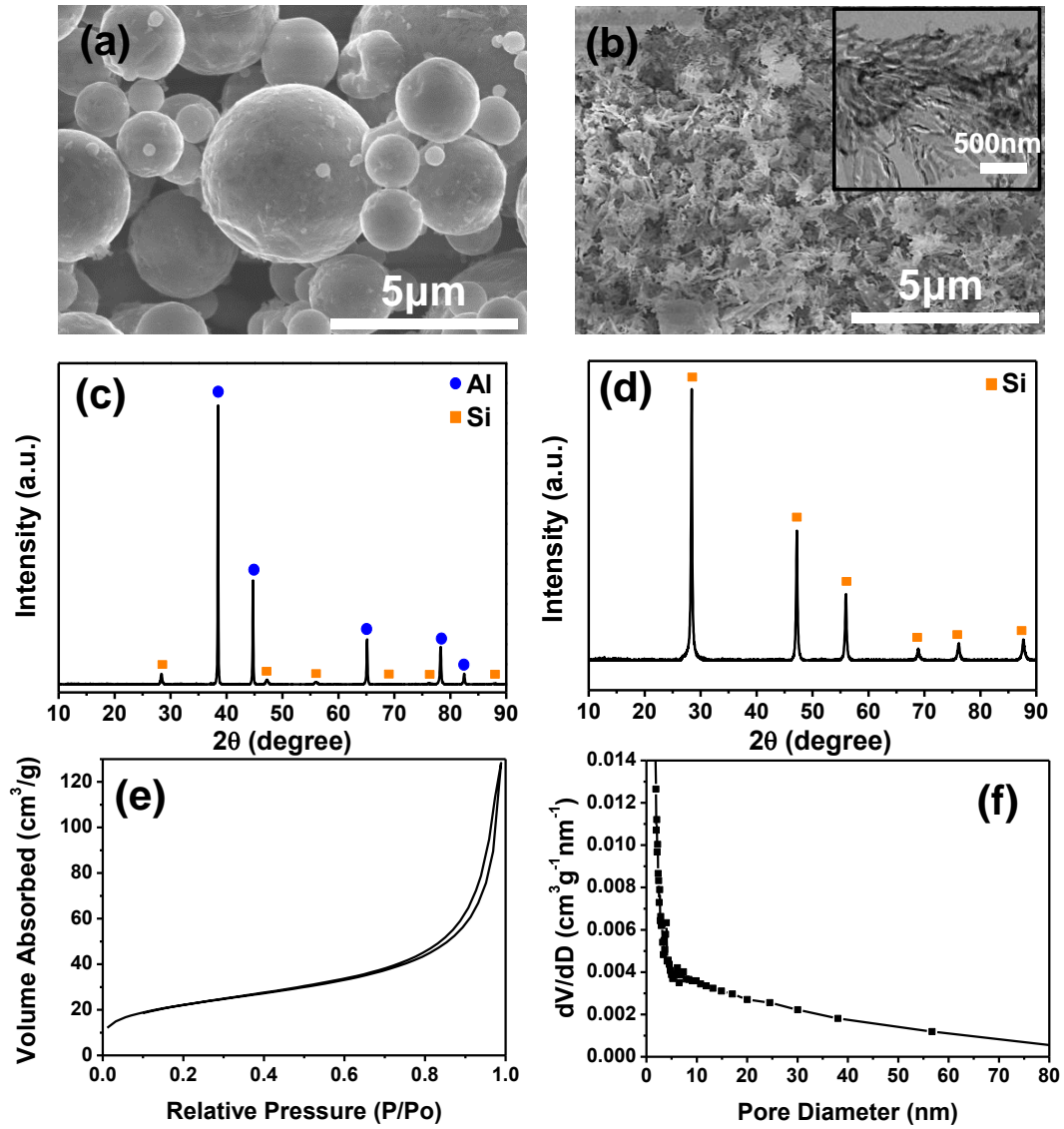


**Figure 2.1.** Characterization of Si foam. SEM images of (a) pristine Al-Si powder and (b) Si foam (inset: TEM image of Si foam with Si frame in range of 50–100 nm.) (c) TEM image and (d) XRD pattern of Si foam. (e) Nitrogen adsorption and desorption isotherm and (f) pore size distribution of Si foam.

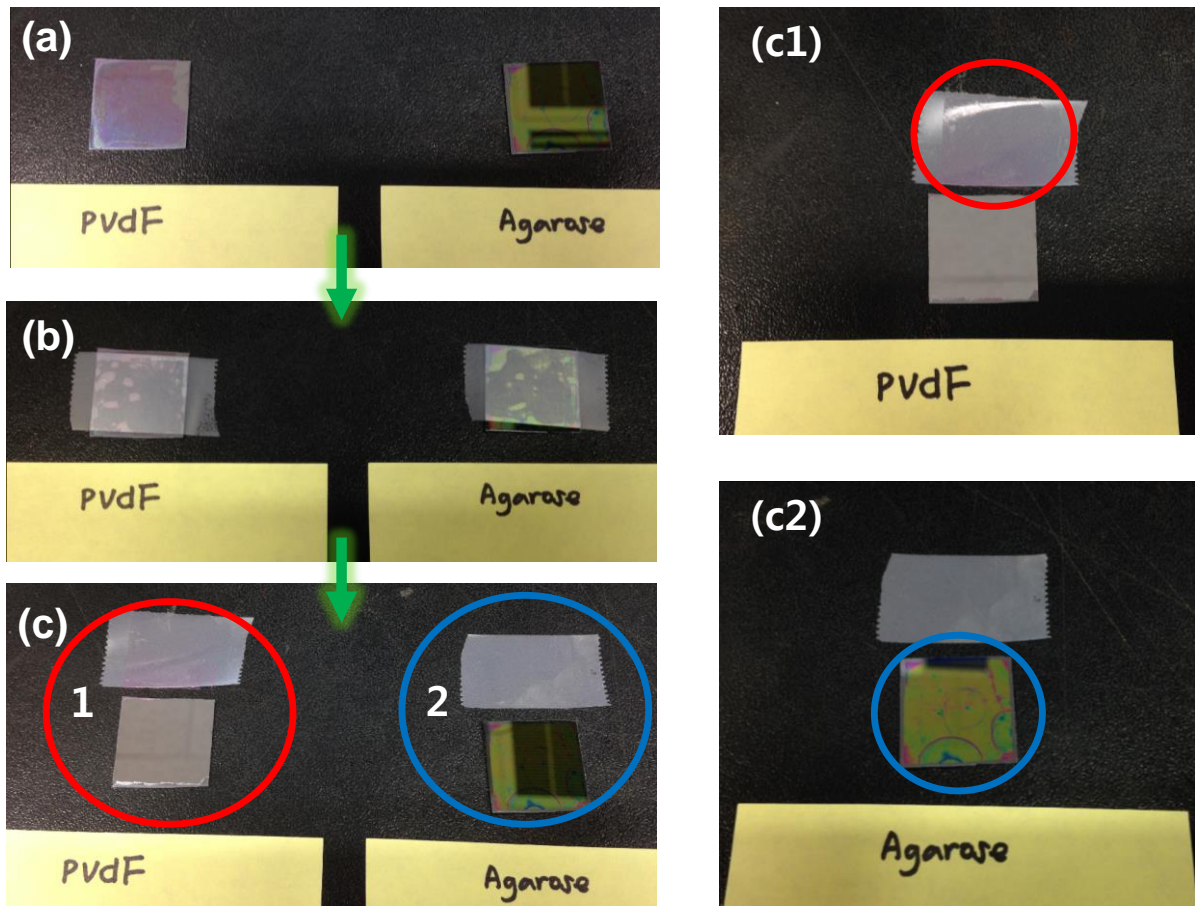


**Figure 2.2.** Peel-off test of PVdF and Agarose binder on Si wafer after spin coating for 2 min at 2000rpm.

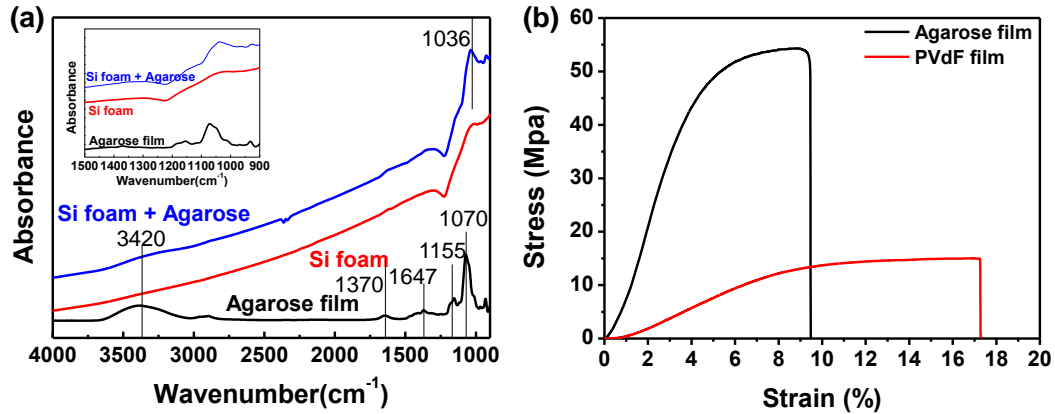


**Figure 2.3.** (a) FT-IR spectra of agarose film, Si foam powder, and electrode consisted of Si foam and agarose. (b) Stress-strain curves of agarose film and PVdF film.

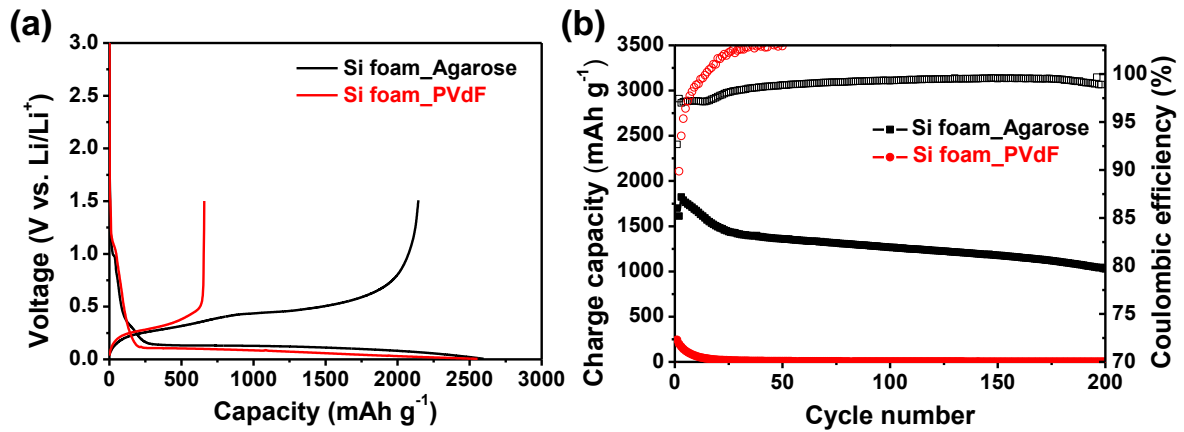


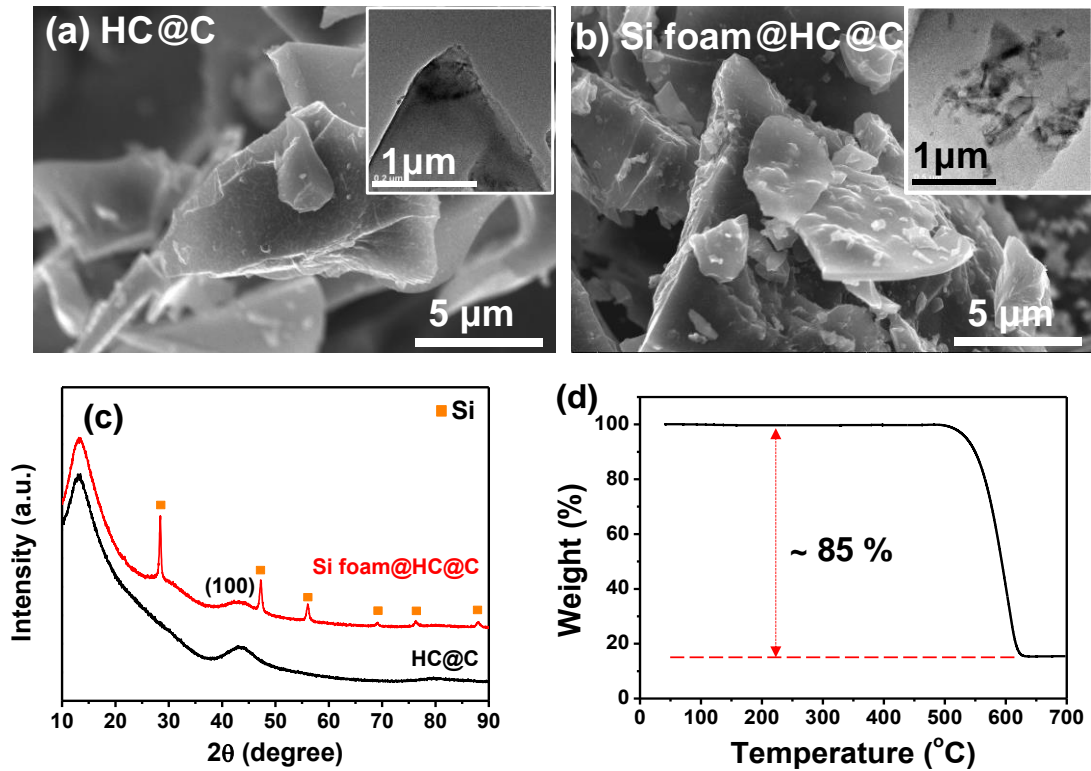
**Figure 2.4.** Electrochemical performance of Si foam using agarose binder and PVdF binder. (a) First cycle voltage profiles in range of 0.005-1.5 V at a rate of C/20. (b) Cycling performance in range of 0.01-1.2V at a rate of 0.2C.

### 3.2. Preparation of HC@C and Si foam@HC@C and its electrochemical test using agarose binder

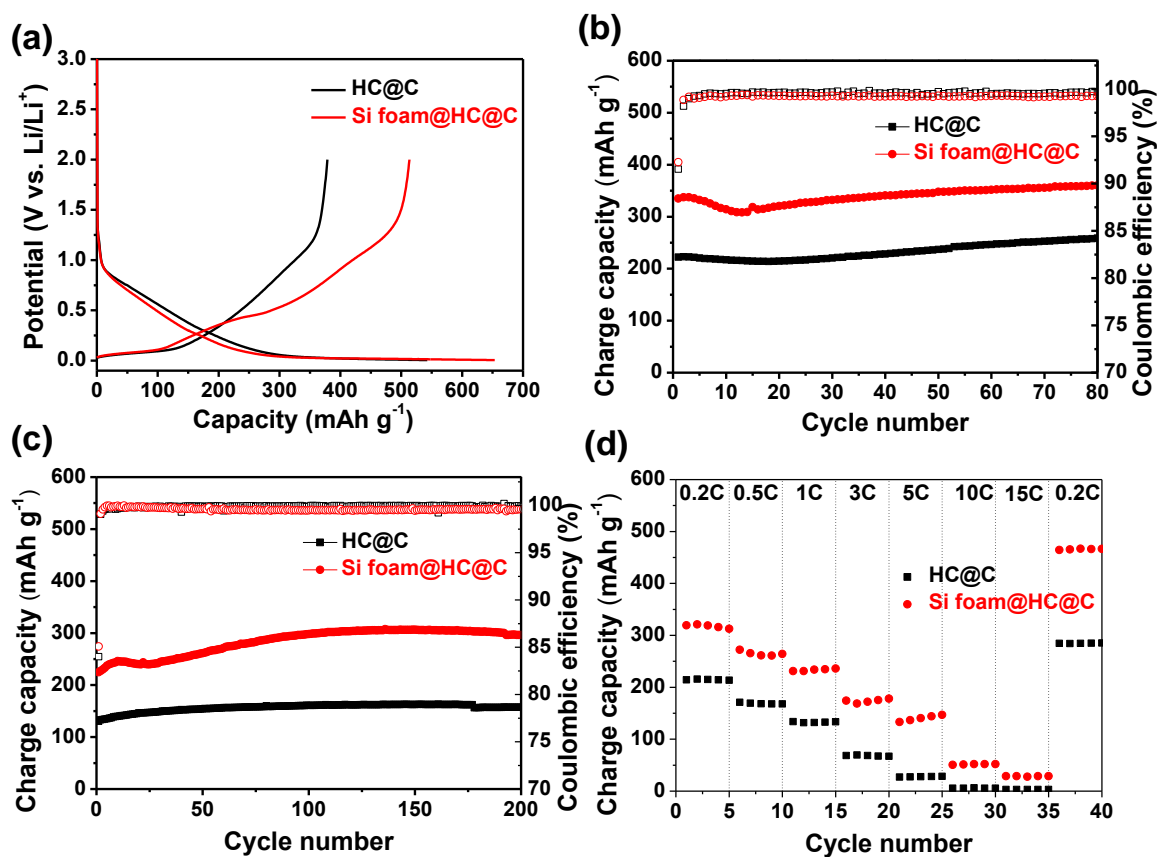
Hard carbon (HC) was prepared by a simple carbonization process of agarose hydrogel (900 °C for 2 h in argon atmosphere). Agarose is linear polysaccharide polymer, generally extracted from seaweeds. Therefore, it is abundant in nature, eco-friendly, and inexpensive material. Since agarose is available as a white powder which dissolves in near-boiling water, and forms a gel when it cools, it can be made into agarose hydrogel. After agarose hydrogel was dried, it was carbonized at 900 °C in argon atmosphere and coated with acetylene gas to increase electrical conductivity and crystallinity. To synthesize Si foam@HC@C, Si foam was dispersed into dimethyl sulfoxide (DMSO), sequentially added agarose powder. After solution was dried completely, obtained material was carbonized and coated with carbon at same condition with HC@C.

Figure 2.5(a) and (b) shows SEM images of as-synthesized HC@C, as-synthesized Si foam@HC@C, respectively. Both of them have flake-type shape with dimension of 1-10  $\mu\text{m}$ . Also, inset TEM images showed flake-like structures of HC@C and Si foam@HC@C. Figure 2.5(c) shows X-ray diffraction (XRD) patterns of both samples. Amorphous carbon peaks of HC@C and Si foam@HC@C are clearly seen in Figure 2.5(c), while the crystalline Si peaks are also shown in the Si foam@HC@C. When we used thermogravimetric analysis (TGA) for the Si foam@HC@C sample, 85 wt% carbon and 15wt% Si were determined, respectively (Figure 2.5(d)).

Electrochemical performance test was conducted by using HC@C and Si foam@HC@C with agarose binder in coin-type half-cell (2016R). The first cycle was carried out in potential range of 0.005-2V at rate of C/20 in shown Figure 2.6(a). The first discharge capacity (lithiation) and discharge capacity (delithiation) of HC@C electrode were 543 and 389 mAh  $\text{g}^{-1}$  with initial coulombic efficiency of 71.6%. In case of Si foam@HC@C electrode, the first discharge capacity and discharge capacity were 654 and 513 mAh  $\text{g}^{-1}$  with initial coulombic efficiency of 78.4%. Cycling performance test was investigated in range of 0.01-1.5V at 0.2C and 1C. Two types of electrodes exhibited gradually increased charge capacity at 0.2C and 1C with increasing cycling numbers, which can be contributed to gradual activation within the structure of hard carbon and silicon, as shown in Figure 2.6(b) and (c). Compared to HC@C, enhanced rate capability of Si foam@HC@C electrodes was displayed in the range of C/5-15C (same discharge/charge rate).



**Figure 2.5.** SEM images of (a) as-synthesized HC@C and (b) Si foam@HC@C. (c) XRD pattern of HC@C and Si foam@HC@C. (Inset: TEM images of HC@C and Si foam@HC@C.) (d) TGA analysis of Si foam@HC@C. This result shows that Si foam@HC@C contains 85 wt% of carbon and 15 wt% of silicon.



**Figure 2.6.** Electrochemical performance of HC@C and Si foam@HC@C electrodes. (a) First cycle voltage profiles obtained at the C/20 rate between 0.005V and 2.0V. Cycle performance of HC@C and Si foam@HC@C at rate of (a) 0.2C and (c) 1C discharge/charge. (d) Rate capability of HC@C and Si foam@HC@C electrodes in the range of C/5-15C (same discharge/charge rate).

### 3.3. Electrochemical performance of $\text{LiMn}_2\text{O}_4$ cathode with agarose binder

Agarose was also used as polymeric binder for  $\text{LiMn}_2\text{O}_4$  (LMO) cathode materials. Electrochemical performance test was carried out in a coin-type half-cell (2016R). The first charge and discharge was investigated in voltage range of 3-4.3V at rate of C/20 in shown Figure 2.7(a). The first charge capacity and discharge capacity of LMO electrode were 105 and 101  $\text{mAh g}^{-1}$  with high initial coulombic efficiency of 96.2%. Agarose did not react with electrolyte in operating voltage (3-4.3V). Cycling stability test was carried out in range of 3-4.3V at 0.2C/0.2C (charge/discharge). Figure 2.7(b) displays stable cycling performance with nearly 100% coulombic efficiency. Compared to conventional PVdF binder, the agarose binder showed a quite comparable electrochemical property.

## 4. Conclusion

We demonstrate eco-friendly, abundant natural polysaccharide as a binder for Si-based anode, Si/C composite materials consisting of the Si foam dispersed in hard carbon (HC) synthesized by using agarose, and  $\text{LiMn}_2\text{O}_4$  cathodes. Si foam@HC@C was successfully synthesized by a simple carbonization method. The nanostructured Si foam and agarose binder containing many functional groups enables to strong adhesion between Si foam and current collector, leading to enhanced electrochemical properties, including a high specific capacity of 1028  $\text{mAh g}^{-1}$  (60% retention compared to 2<sup>nd</sup> cycle) and outstanding cycling performance after 200 cycles. Si foam@HC@C electrode showed first discharge capacity and discharge capacity were 654 and 513  $\text{mAh g}^{-1}$  with enhanced initial coulombic efficiency of 78.4%, compared to HC@C with initial coulombic efficiency of 71.6%.  $\text{LiMn}_2\text{O}_4$  cathode with agarose binder exhibited high initial coulombic efficiency of 96.2% and stable cycling performance with nearly 100% coulombic efficiency. These results indicate agarose binder can be used for both of anode and cathode due to good electrochemical stability in wide operating voltage.

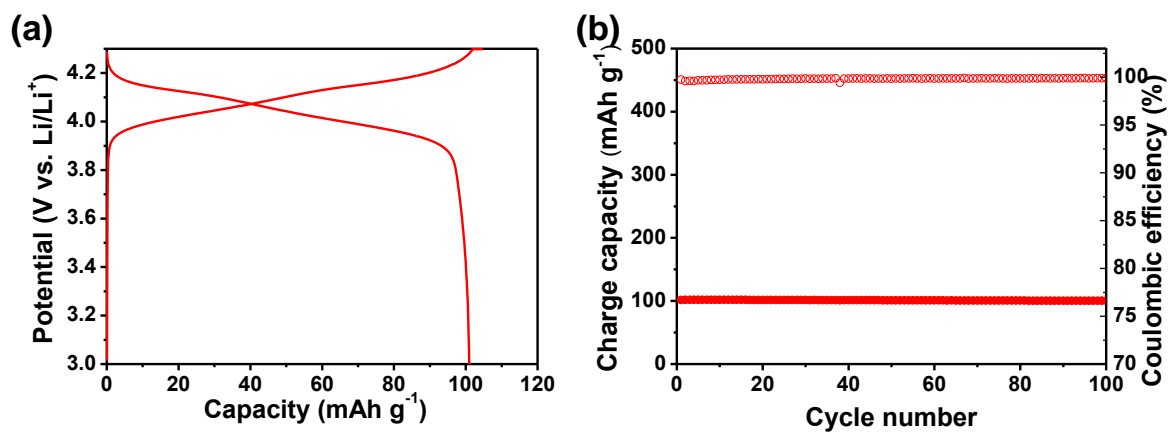


**Figure 2.7.** (a) First charge and discharge voltage profile in voltage range of 3-4.3V at rate of C/20. (b) Cycling stability test in range of 3-4.3V at 0.2C/0.2C (charge/discharge).



## 5. References

1. J.-M. T. a. M. Armand, Issues and challenges facing rechargeable lithium batteries. *Nature* **2001**, *414* (6861), 359-367.
2. F. Cheng, J. Liang, Z. Tao and J. Chen, Functional materials for rechargeable batteries. *Adv. Mater.* **2011**, *23* (15), 1695-1715.
3. H. K. Bruce Dunn, Jean-Marie Tarascon, Electrical energy storage for the grid: a battery of choices. *Science* **2011**, *334* (6058), 928-935.
4. V. Etacheri, R. Marom, R. Elazari, G. Salitra and D. Aurbach, Challenges in the development of advanced Li-ion batteries: a review. *Energy Environ. Sci.* **2011**, *4* (9), 3243.
5. M. R. Palacin, Recent advances in rechargeable battery materials: a chemist's perspective. *Chem. Soc. Rev.* **2009**, *38* (9), 2565-2575.
6. B. Scrosati, Recent advances in lithium ion battery materials. *Electrochim. Acta* **2000**, *45* (15), 2461-2466.
7. C. M. Park, J. H. Kim, H. Kim and H. J. Sohn, Li-alloy based anode materials for Li secondary batteries. *Chem. Soc. Rev.* **2010**, *39* (8), 3115-3141.
8. U. Kasavajjula, C. Wang and A. J. Appleby, Nano- and bulk-silicon-based insertion anodes for lithium-ion secondary cells. *J. Power Sources* **2007**, *163* (2), 1003-1039.
9. A. Magasinski, P. Dixon, B. Hertzberg, A. Kvit, J. Ayala and G. Yushin, High-performance lithium-ion anodes using a hierarchical bottom-up approach. *Nature materials* **2010**, *9* (4), 353-358.
10. C. K. Chan, H. Peng, G. Liu, K. McIlwrath, X. F. Zhang, R. A. Huggins and Y. Cui, High-performance lithium battery anodes using silicon nanowires. *Nat. Nanotechnol.* **2007**, *3* (1), 31-35.
11. S. P. V. Nadimpalli, V. A. Sethuraman, S. Dalavi, B. Lucht, M. J. Chon, V. B. Shenoy and P. R. Guduru, Quantifying capacity loss due to solid-electrolyte-interphase layer formation on silicon negative electrodes in lithium-ion batteries. *J. Power Sources* **2012**, *215*, 145-151.
12. S. Dalavi, P. Guduru and B. L. Lucht, Performance Enhancing Electrolyte Additives for Lithium Ion Batteries with Silicon Anodes. *J. Electrochem. Soc.* **2012**, *159* (5), A642.
13. V. Etacheri, O. Haik, Y. Goffer, G. A. Roberts, I. C. Stefan, R. Fasching and D. Aurbach, Effect of fluoroethylene carbonate (FEC) on the performance and surface chemistry of Si-nanowire Li-ion battery anodes. *Langmuir* **2012**, *28* (1), 965-976.
14. R. Huang, X. Fan, W. Shen and J. Zhu, Carbon-coated silicon nanowire array films for high-performance lithium-ion battery anodes. *Appl. Phys. Lett.* **2009**, *95* (13), 133119.
15. S. Choi, J. C. Lee, O. Park, M.-J. Chun, N.-S. Choi and S. Park, Synthesis of micro-assembled

- Si/titanium silicide nanotube anodes for high-performance lithium-ion batteries. *J. Mater. Chem. A* **2013**, *1* (36), 10617.
16. C.-H. Yim, F. M. Courtel and Y. Abu-Lebdeh, A high capacity silicon–graphite composite as anode for lithium-ion batteries using low content amorphous silicon and compatible binders. *J. Mater. Chem. A* **2013**, *1* (28), 8234.
  17. D. Shao, D. Tang, Y. Mai and L. Zhang, Nanostructured silicon/porous carbon spherical composite as a high capacity anode for Li-ion batteries. *J. Mater. Chem. A* **2013**, *1* (47), 15068.
  18. L. Hu, H. Wu, S. S. Hong, L. Cui, J. R. McDonough, S. Bohy and Y. Cui, Si nanoparticle-decorated Si nanowire networks for Li-ion battery anodes. *Chem. Commun.* **2011**, *47* (1), 367-369.
  19. C. K. Chan, R. Ruffo, S. S. Hong, R. A. Huggins and Y. Cui, Structural and electrochemical study of the reaction of lithium with silicon nanowires. *J. Power Sources* **2009**, *189* (1), 34-39.
  20. M.-H. Park, M. G. Kim, J. Joo, K. Kim, J. Kim, S. Ahn, Y. Cui and J. Cho, Silicon Nanotube Battery Anodes. *Nano Lett.* **2009**, *9* (11), 3844-3847.
  21. W.-R. Liu, M.-H. Yang, H.-C. Wu, S. M. Chiao and N.-L. Wu, Enhanced Cycle Life of Si Anode for Li-Ion Batteries by Using Modified Elastomeric Binder. *Electrochem. Solid-State Lett.* **2005**, *8* (2), A100.
  22. L. Xie, L. Zhao, J.-l. Wan, Z.-q. Shao, F.-j. Wang and S.-y. Lv, The Electrochemical Performance of Carboxymethyl Cellulose Lithium as a Binding Material for Anthraquinone Cathodes in Lithium Batteries. *J. Electrochem. Soc.* **2012**, *159* (4), A499.
  23. N.-S. Choi, K. H. Yew, W.-U. Choi and S.-S. Kim, Enhanced electrochemical properties of a Si-based anode using an electrochemically active polyamide imide binder. *J. Power Sources* **2008**, *177* (2), 590-594.
  24. A. Magasinski, B. Zdyrko, I. Kovalenko, B. Hertzberg, R. Burtovyy, C. F. Huebner, T. F. Fuller, I. Luzinov and G. Yushin, Toward efficient binders for Li-ion battery Si-based anodes: polyacrylic acid. *ACS Appl. Mater. Interfaces* **2010**, *2* (11), 3004-3010.
  25. B. Z. Igor Kovalenko, Alexandre Magasinski, Benjamin Hertzberg, Zoran ilicev, and I. L. Ruslan Burtovyy, Gleb Yushin, A major constituent of brown algae for use in high-capacity Li-ion batteries. *Science* **2011**, *334* (6052), 75-79.
  26. Z.-J. Han, N. Yabuuchi, K. Shimomura, M. Murase, H. Yui and S. Komaba, High-capacity Si–graphite composite electrodes with a self-formed porous structure by a partially neutralized polyacrylate for Li-ion batteries. *Energy Environ. Sci.* **2012**, *5* (10), 9014.
  27. B. Koo, H. Kim, Y. Cho, K. T. Lee, N. S. Choi and J. Cho, A highly cross-linked polymeric binder for high-performance silicon negative electrodes in lithium ion batteries. *Angew. Chem. Int. Ed. Engl.* **2012**, *51* (35), 8762-8767.

28. C. Kim, J. Y. Jang, N.-S. Choi and S. Park, Multi-functionalities of natural polysaccharide for enhancing electrochemical performance of macroporous Si anodes. *RSC Adv.* **2014**, *4* (6), 3070.
29. Y. K. Jeong, T. W. Kwon, I. Lee, T. S. Kim, A. Coskun and J. W. Choi, Hyperbranched beta-Cyclodextrin Polymer as an Effective Multidimensional Binder for Silicon Anodes in Lithium Rechargeable Batteries. *Nano Lett.* **2014**, *14* (2), 864-870.
30. T. R. J. S.S. Zhang, Study of poly (acrylonitrile-methyl methacrylate) as binder for graphite anode and LiMn<sub>2</sub>O<sub>4</sub> cathode of Li-ion batteries. *J. Power Sources* **2002**, *109* (2), 422-426.
31. S. Lee, E.-Y. Kim, H. Lee and E.-S. Oh, Effects of polymeric binders on electrochemical performances of spinel lithium manganese oxide cathodes in lithium ion batteries. *J. Power Sources* **2014**, *269*, 418-423.
32. M.-H. Ryou, S. Hong, M. Winter, H. Lee and J. W. Choi, Improved cycle lives of LiMn<sub>2</sub>O<sub>4</sub> cathodes in lithium ion batteries by an alginate biopolymer from seaweed. *J. Mater. Chem. A* **2013**, *1* (48), 15224.
33. K.-F. Chiu, S. H. Su, H.-J. Leu and Y. S. Chen, Application of lithiated perfluorosulfonate ionomer binders to enhance high rate capability in LiMn<sub>2</sub>O<sub>4</sub> cathodes for lithium ion batteries. *Electrochim. Acta* **2014**, *117*, 134-138.

## Chapter III. A High-performance Nanoporous Si/Al<sub>2</sub>O<sub>3</sub> Foam Lithium-ion Battery anode

### 1. Introduction

Silicon (Si) is one of the most attractive anode materials for rechargeable lithium-ion batteries (LIBs) owing to its abundance in nature, low cost, relatively low working potential (< 0.4 versus Li/Li<sup>+</sup>) and high theoretical capacity (3579 mA h g<sup>-1</sup> with composition of Li<sub>15</sub>Si<sub>4</sub> at room temperature).<sup>1, 2</sup> However, the large volume change of Si (> 300%) during the Li insertion/extraction process gives rise to pulverization of Si electrodes, the formation of an unstable thick solid-electrolyte-interface (SEI) layer, and acceleration of electrolyte depletion, resulting in serious capacity fading. These problems hinder commercial use of Si anode materials in LIBs.

In order to overcome these problems, numerous strategies have been developed to release the large strain and stress that occur during the cycling of Si anodes, by introducing concepts of nanostructuring, such as nanoparticles,<sup>3</sup> nanowires,<sup>4</sup> nanotubes<sup>5</sup> and nanocomposites.<sup>6, 7</sup> For example, Chan et al. demonstrated that Si nanowires can prevent the initiation of fractures because the small nanowire diameter can endure a large volume change.<sup>7</sup> Zhou et al.<sup>8</sup> and Jiang et al.<sup>9</sup> proposed a simple and cost-effective method to synthesize nanostructured porous Si by hydrochloric acid etching of Al–Si alloy particles. They showed that the nanostructured Si is effective in improving electrochemical performances because the reduced dimension both increases the rate of lithium insertion/extraction owing to the short distance for Li-ion transport within the particles and also enhances the electron transport within the particles. However, a large portion of polymeric binders was used and initial coulombic efficiency (ICE) was low due to a side reaction of the Al–Si electrode and the electrolyte.

Introducing protection layers on the surface of various structured Si particles has been suggested as another effective method to reduce the side reaction and to form stable SEI layers on the Si surface. For example, carbon,<sup>10</sup> metal,<sup>11</sup> metal oxide,<sup>12</sup> metal silicide,<sup>13, 14</sup> and conducting polymer coating layers<sup>15</sup> have been introduced on the Si surface to maintain the original Si structure and to enhance electrical conductivity. Among these materials, Al<sub>2</sub>O<sub>3</sub> deposited by the atomic layer deposition (ALD) method has been studied as a protection layer on the Si surface.<sup>16, 17</sup> It showed significantly improved cycling performance due to the suppression of the side reaction between Si and the electrolyte by the thin Al<sub>2</sub>O<sub>3</sub> layer. However, the ALD process is not a cost-effective way for large-scale production of Si-based materials.

Herein, we demonstrate a simple and cost-effective synthesis of micron-scale nanostructured Si/Al<sub>2</sub>O<sub>3</sub> foam particles from the Al–Si alloy by combining chemical etching with a selective thermal oxidation process. The amount of Al is controlled by the etching time and subsequent preferential thermal oxidation of Al layers leads to the formation of Si/Al<sub>2</sub>O<sub>3</sub> foam. As-synthesized Si/Al<sub>2</sub>O<sub>3</sub> foam

is tested as an LIB anode. It exhibits outstanding cycling stability (a capacity retention of 78% after 300 cycles at the  $C/5$  rate), excellent rate capability, and suppressed volume expansion after long-term cycling.

## 2. Experimental

### 2.1 Synthesis of Si/Al<sub>2</sub>O<sub>3</sub> Foam

**Preparation of nanostructured micrometer sized Al-Si powder:** 13.0 g Al-Si alloy powder (325 mesh, 99%, Al:Si = 88:12 wt.%, Alfa Aesar) was immersed in 400 mL of 3 M hydrochloric acid (HCl) solution (SAMCHUN chemical, Korea) for 30 min with stirring. The chemically etched powder was filtered, washed several times with deionized (DI) water and dried at 70 °C for 12 hr. At this condition, we obtained the production yield of 18%.

**Synthesis of Si/Al<sub>2</sub>O<sub>3</sub> foam particles:** To oxidize residual Al in the chemically etched Al-Si particles, 0.35 g of the etched Al-Si powder was thermally oxidized with water vapor as an oxidant at 600 °C for 10, 30 and 60 min. The water vapor was supplied into the tube furnace by bubbling DI water assisted with N<sub>2</sub> gas (5 L min<sup>-1</sup>).

### 2.2 Characterization

Scanning electron microscopy (SEM, S-4800, Hitachi) at an accelerating voltage of 10kV and high-resolution transmission electron microscopy (HR-TEM, JEOL, JEM-2100F) operating at 200kV were used to characterize morphologies and element mapping of Al-Si and Si/Al<sub>2</sub>O<sub>3</sub> samples. To investigate the microstructures of samples, X-ray diffractometer (XRD, D8 Advance, Bruker, Cu K $\alpha$  radiation) was used between 10 and 90° at a scan rate of 1.4° sec<sup>-1</sup>.

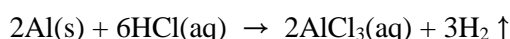
### 2.3 Electrochemical measurements

To evaluate electrochemical performances of chemically etched and thermally oxidized samples, the electrodes were prepared by mixing 70 wt% active material (etched Al-Si powder, thermally oxidized Si/Al<sub>2</sub>O<sub>3</sub> powder), 20 wt% of super P and 10 wt% of binder (poly(acrylic acid)/sodium carboxymethyl cellulose (PAA:CMC = 1:1, w/w)) with a mixer (Thinky mixer, ARE310) at 2200 rpm for 15 min to homogenize slurry. After the slurries were casted on a copper foil, the electrodes were dried at 150 °C for 2 hr in a vacuum oven to solidify electrodes. The mass loading level of active materials in electrodes was around 0.9 mg cm<sup>-2</sup>. The coin-type half-cell (2016R) was assembled in an Ar-filled glove box with oxygen and water less than 1 ppm. The Li metal foil was used as counter electrode and micro porous polyethylene film (Celgard 2400) was used as a separator. The electrolyte consisted of a solution of 1.3M LiPF<sub>6</sub> in a mixture of ethylene carbonate (EC)/diethyl carbonate (DEC) (3:7, v/v) with 10% fluorinated ethylene carbonate (FEC) additive. Galvanostatic charge and discharge cycling (WonATech WBCS 3000 battery measurement system) was performed between 0.005 and 1.2 V (versus Li/Li+) at 25 °C. For the chemically etched (30 min) Al-Si, 10 min-, 30 min-, and 60 min- oxidized Si/Al<sub>2</sub>O<sub>3</sub> electrodes, 1C rate is 2.1, 1.4, 1.0, and 0.8 A/g, respectively.

After cycling, the cells were disassembled in a glove box and the electrodes were rinsed with dimethyl carbonate (DMC) for 1 h to remove residual electrolytes and dried at room temperature. The AC impedance analysis was obtained using IVIUM frequency response analyzer ranging from 0.01 Hz to 100 kHz.

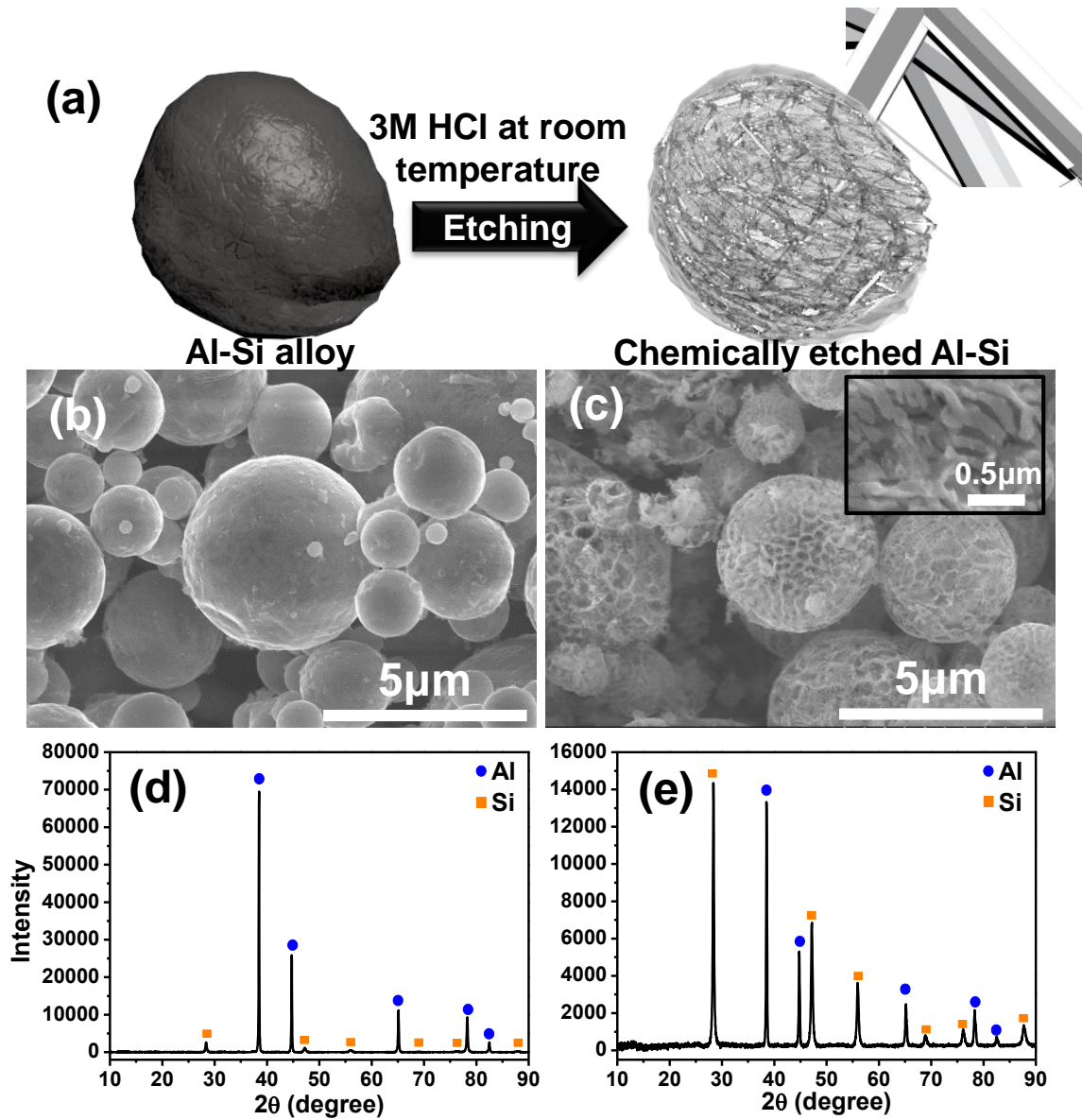
### 3. Results and discussion

Micro-scale nanostructured Al–Si foam was prepared by acid etching of Al–Si alloy powder (Figure 3.1a). The hydrochloric acid (HCl) etchant preferentially attacks Al, resulting in the formation of a foam-type Si structure (including a small amount of remaining Al depending on the etching conditions) without a serious collapse. The following equation shows the etching reaction with Al and HCl.



A scanning electron microscopy (SEM) image of pristine Al–Si powder shows that the particle diameters are in the range of 1–6  $\mu\text{m}$  (Figure 3.1b). When the Al–Si particles (13 g) were etched in 3 M HCl at room temperature for 30 min, an Al–Si foam-like structure with a Si frame of 50–100 nm was obtained (Figure 3.1c). Microstructures of pristine (Fig. 1d) and the chemically etched Al–Si particles (Figure 3.1e) were investigated by X-ray diffraction (XRD) patterns. After chemical etching, the peak intensity of Al was significantly decreased (around 5 times lower than that of the pristine sample). To characterize the amount of Al and Si in both samples, energy-dispersive X-ray spectroscopy (EDS) was employed. The pristine Al–Si powders contain 85 wt% of Al and 11 wt% of Si, while the etched sample shows 21 wt% Al and 67 wt% Si because of a selective etching of Al parts (Figure 3.2 and Table 3.1). Al contents ranging from 60 wt% to 4 wt% can be easily tuned by controlling the etching time from 15 to 60 min under the same etching conditions (Table 3.1). Among various Al–Si foam particles, we selected the 30 min-etched sample as a model system for making Si/Al<sub>2</sub>O<sub>3</sub> foam particles, because the 10 min-etched sample was partially etched and the 60 min-etched particle was seriously etched away with a destruction of the original structure (Figure 3.3).

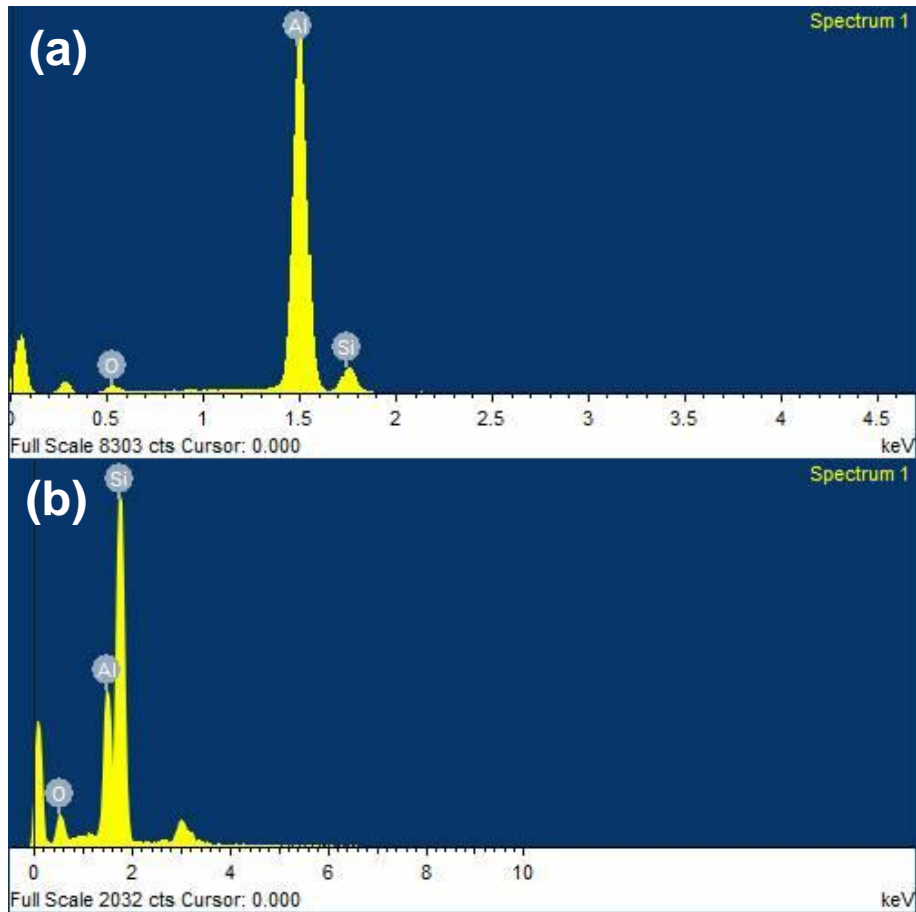




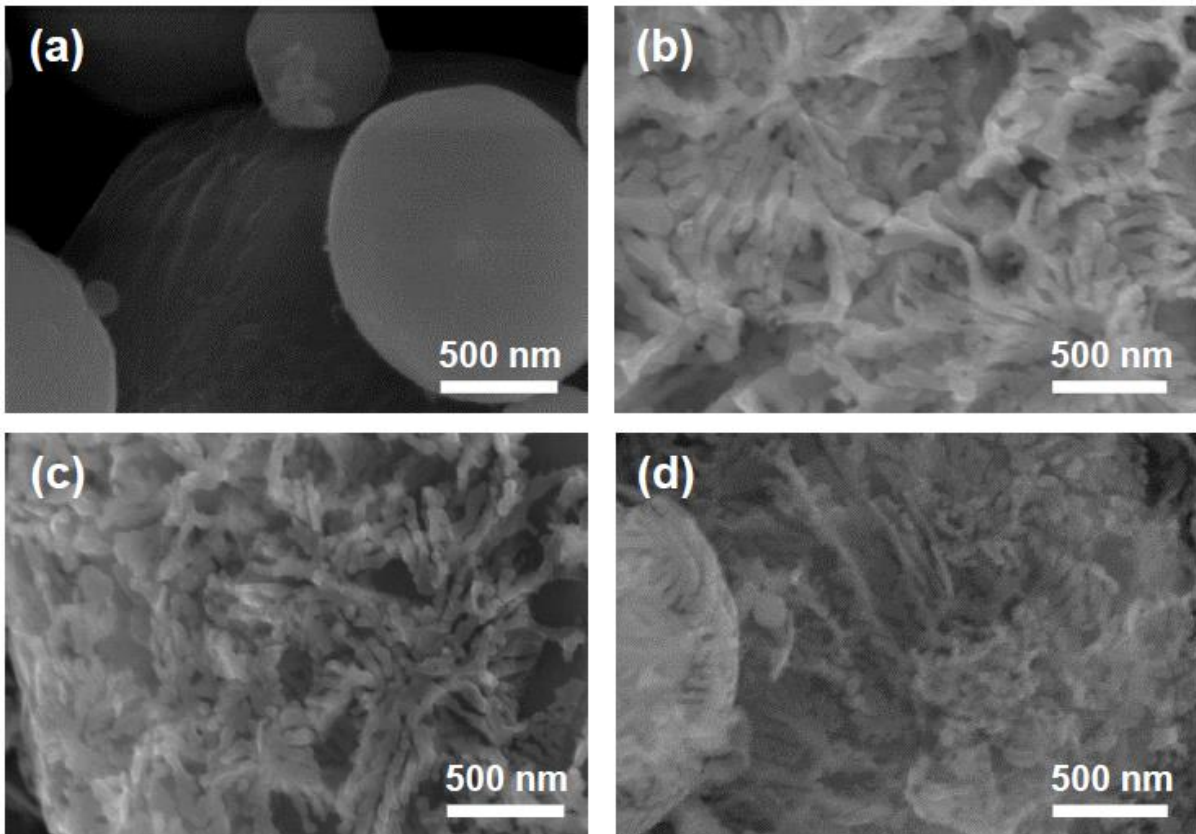
**Figure 3.1.** (a) Schematic illustration showing the synthetic process of Al-Si foam-like particles. SEM images of (b) pristine Al-Si alloy and (c) chemically etched Al-Si powder. XRD patterns of (d) Al-Si alloy and (e) chemically etched Al-Si powder.

**Table 3.1.** EDS data of the amount of elements depending on etching time.

Elements	Before etching	15 min	30 min	45 min	60 min
	Weight%	Weight%	Weight%	Weight%	Weight%
O	4.45	5.88	11.45	12.90	12.56
Al	84.69	60.58	21.10	7.58	4.28
Si	10.87	33.54	67.45	79.53	83.16



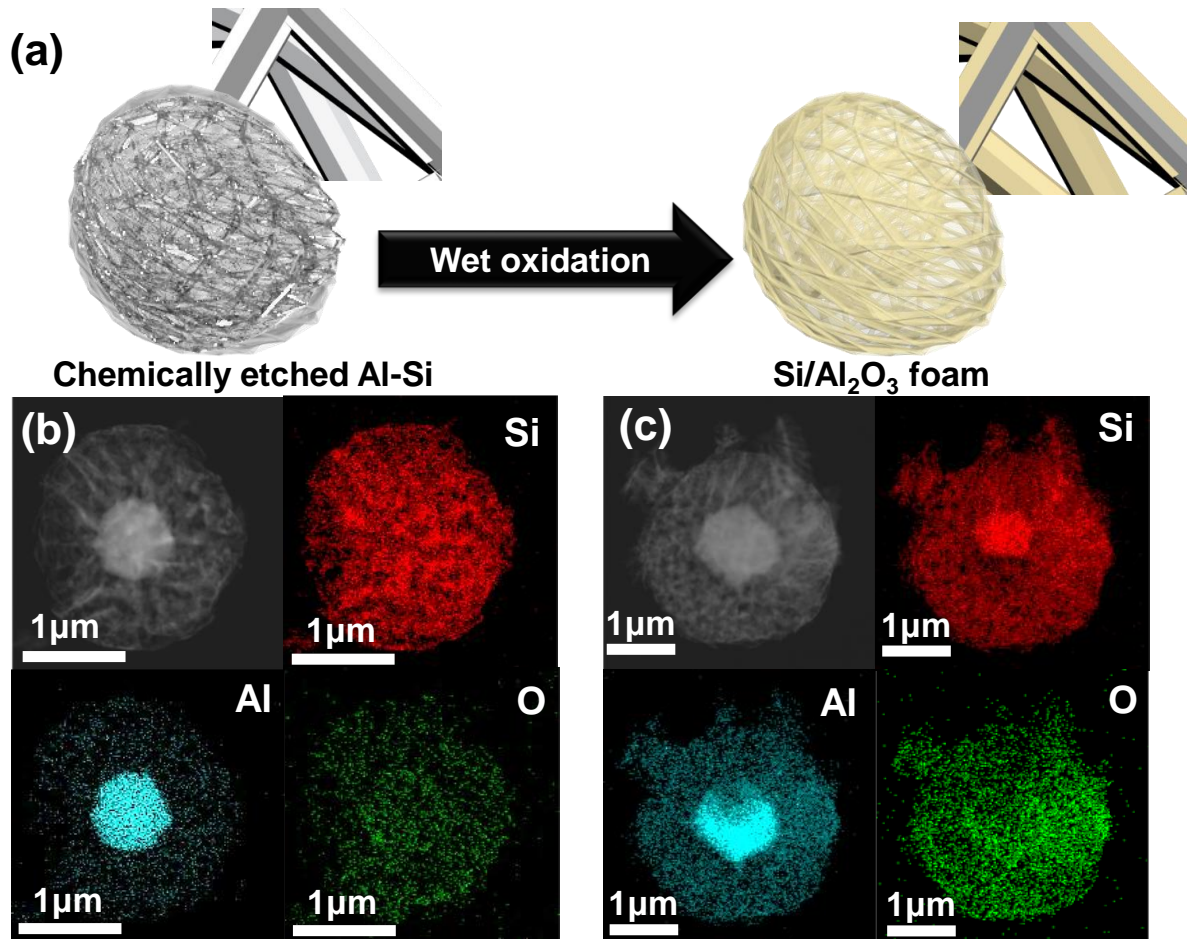
**Figure 3.2.** EDS spectra of (a) Al-Si alloy powder and (b) chemically etched Al-Si powder.



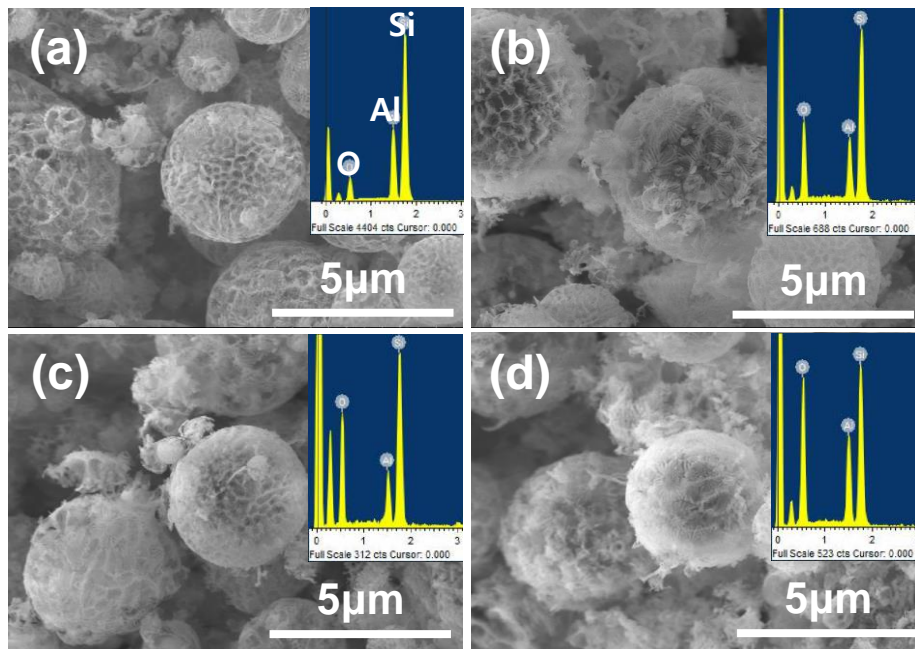
**Figure 3.3.** SEM images of chemically etched Al-Si particles for (a) 10 min, (b) 30 min, (c) 45 min, and (d) 60 min at room temperature.

Figure 3.4a illustrates the synthesis of Si/Al<sub>2</sub>O<sub>3</sub> foam particles fabricated by the selective oxidation of Al by a thermal oxidation process performed at 600 °C with controlled water vapour. High-angle annular dark-field scanning transmission electron microscopy (HAADF-STEM) and the corresponding EDS mapping images of chemically etched Al–Si and the thermally oxidized (10 min) sample show that thin Al<sub>2</sub>O<sub>3</sub> layers are coated on the Si frame in the outer shell, while Al<sub>2</sub>O<sub>3</sub> particles of 500–600 nm diameter are located in the core of the Si/Al<sub>2</sub>O<sub>3</sub> foam as major components (Figure 3.4b). This can be explained as follows: the diffusion rate of the chemical etchant gradually decreases from the surface to the core, so that a large amount of Al is etched out of the outer shell, but most of the Al is still intact in the core regions.

To convert residual Al to Al<sub>2</sub>O<sub>3</sub>, a thermal oxidation process of chemically etched (30 min) Al–Si powder was performed at 600 °C for three different periods of time. The etched Al–Si powders were exposed to water vapour at 600 °C for 10, 30, and 60 min to control the thickness of the Al<sub>2</sub>O<sub>3</sub> layers. It should be noted that the Si species was not easily oxidized at 600 °C even in a wet atmosphere.<sup>18, 19</sup> After the oxidation process, the amount of oxygen was increased for all three samples, while the original foam-like structure was maintained because thermal oxidation was performed at well below the melting temperature of Al (T<sub>m</sub> = 660.32 °C) (Figure 3.4c and Figure 3.5). Also, XRD patterns of the chemically etched and thermally oxidized samples show that the peak intensity of pure Al is gradually decreased with increasing oxidation time (Figure 3.6). However, XRD patterns of newly developed Al<sub>2</sub>O<sub>3</sub> are not clearly seen, because thermal oxidation of Al at low temperature leads to the formation of amorphous Al<sub>2</sub>O<sub>3</sub>.<sup>20, 21</sup> To investigate the oxidation rate of Si and Al, we used pure Si nanoparticles (an average diameter of 100 nm) and pure Al particles (3 μm) under the same thermal oxidation conditions. The SiO<sub>2</sub> layers on the Si surface were grown with a thickness of ~ 3 nm after thermal oxidation for 60 min, while amorphous Al<sub>2</sub>O<sub>3</sub> layers of ~6 nm were formed on the Al surface at 600 °C for 10 min (Figure 3.7). As another control experiment, the thermal oxidation process of Al particles was monitored by XRD patterns. When the Al particles were thermally oxidized at 600 °C for 10 min, 30 min, and 60 min, Al<sub>2</sub>O<sub>3</sub> layers of 20%, 25%, and 35% were formed, respectively (Figure 3.8). Furthermore, we investigated the Brunauer–Emmett–Teller (BET) surface area of the etched Al–Si particle (29.2 m<sup>2</sup> g<sup>-1</sup>) and the thermally oxidized sample (10 min, 22.1 m<sup>2</sup> g<sup>-1</sup>) (Figure 3.9).



**Figure 3.4.** (a) Schematic illustration showing the thermal oxidation process of chemically etched Al-Si particles. HAADF-STEM and the corresponding EDS mapping images of (b) etched Al-Si powder and (c) thermally oxidized (10 min) Al-Si powder.



**Figure 3.5.** SEM images and EDS spectra of (a) chemically etched Al-Si powder and Si/Al<sub>2</sub>O<sub>3</sub> particles thermally oxidized for (b) 10 min, (c) 30 min, and (d) 60 min.

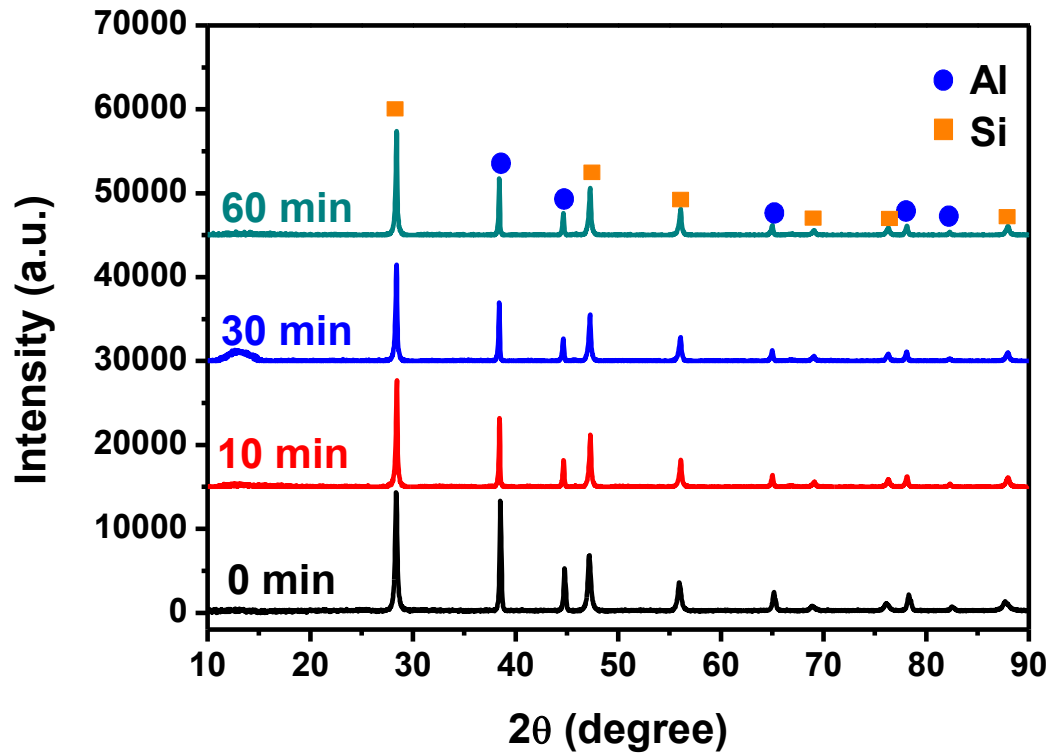


**Figure 3.6.** XRD patterns of chemically etched Al-Si and three different thermally oxidized Al-Si powders.

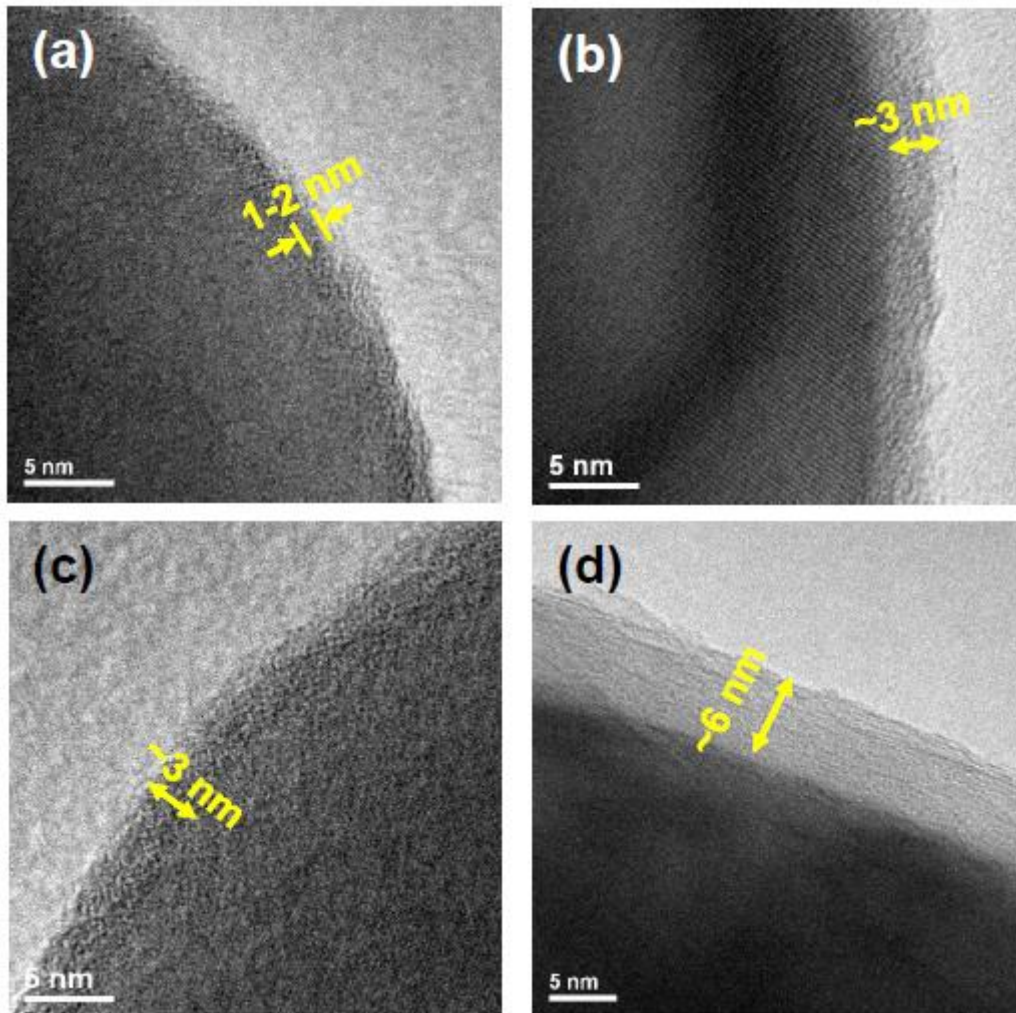


**Figure 3.7.** TEM images of thermally oxidized samples at 600 °C: Thermally oxidized Si for (a) 10 min, (b) 30 min, (c) 60 min and (d) thermally oxidized Al sample for 10 min. In the case Al particle, we used micrometer-sized Al (an average particle size of 3  $\mu\text{m}$ ). After thermal oxidation at 600 °C for 10 min, a focused-ion beam technique was employed to obtain sectioned sample for TEM measurement.



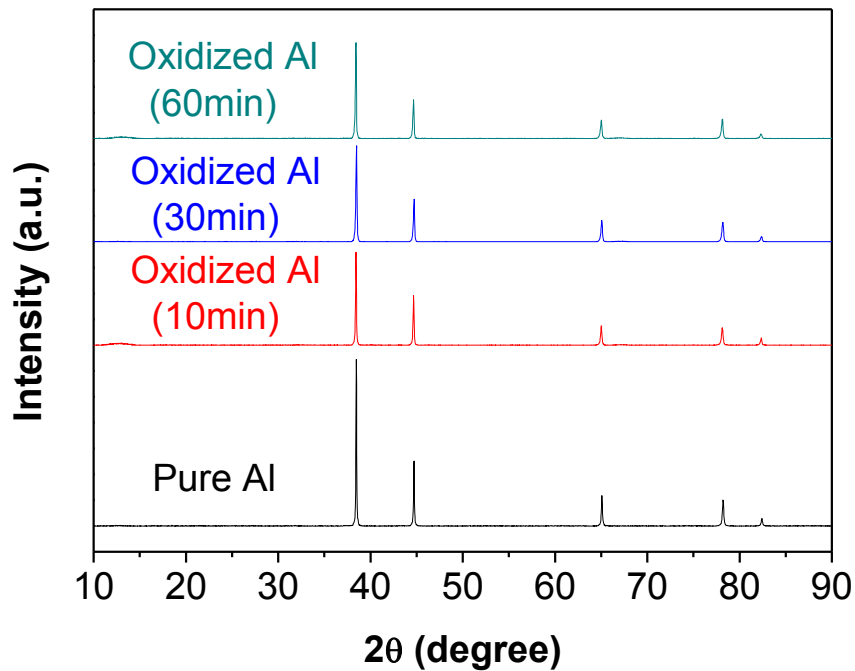


**Figure 3.8.** XRD patterns of pure Al and samples thermally oxidized at 600 °C for 10 min (red), 30 min (blue), and 60 min (cyan). As the oxidation time increased, the Al peak was gradually decreased. From the first order scattering peak of each sample, we estimated the  $\text{Al}_2\text{O}_3$  contents from the Al contents remained after the thermal oxidation. When the pure Al was thermally oxidized for 10 min, 30 min, and 60 min, the  $\text{Al}_2\text{O}_3$  layers of 20%, 25%, and 35% were formed on the Al surface, respectively. It should be noted that the Al of 65% was still left, even though the pure micrometer-sized Al particles was oxidized at 600 °C for 60 min.

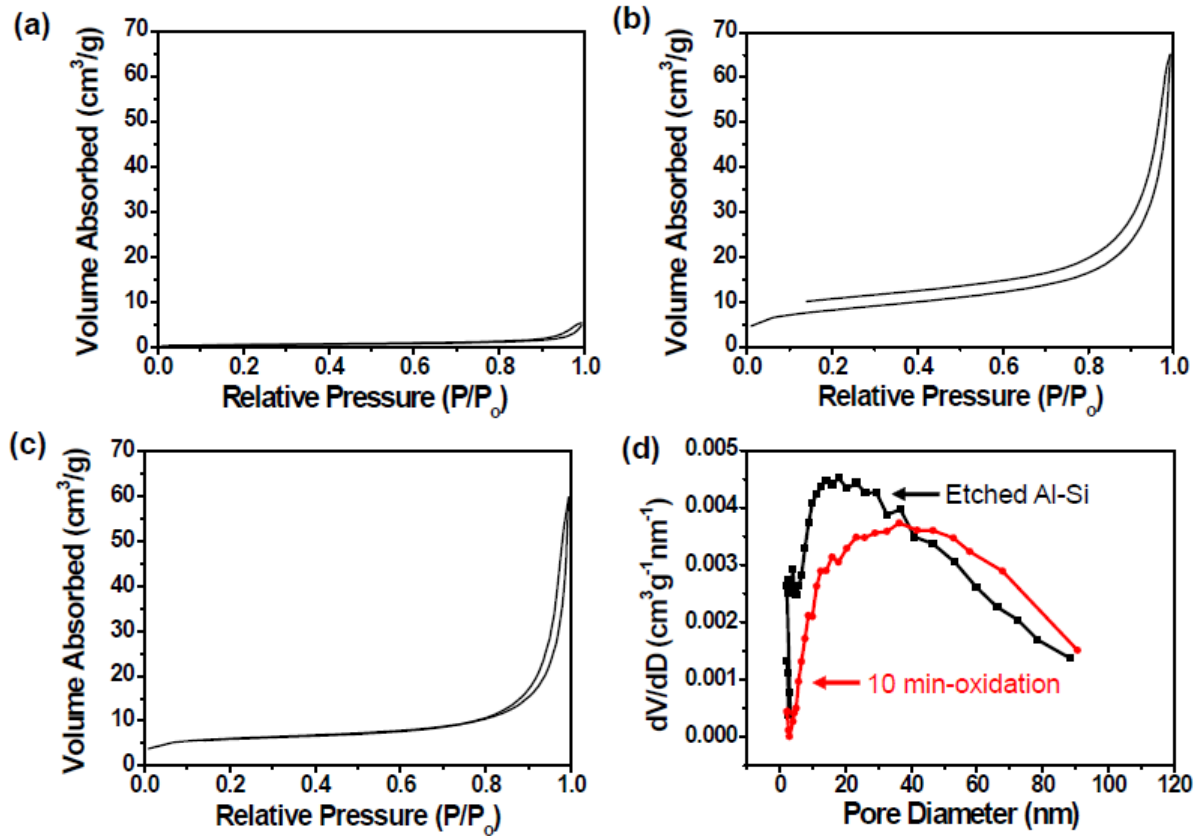


**Figure 3.9.** BET surface area of (a) pristine Al-Si alloy, (b) 30 min-etched Al-Si, and (c) 10 min thermally oxidized Si/ $\text{Al}_2\text{O}_3$ . (d) Pore size distribution of the chemically etched and 10 min oxidized particles.

From these results, we can say that the  $\text{Al}_2\text{O}_3$  layers were successfully introduced on the Si surface with controlled thickness. Since the Si/ $\text{Al}_2\text{O}_3$  foam particles have many void spaces which can act as buffer layers for the large volume change of Si electrodes, and provide  $\text{Al}_2\text{O}_3$  protecting layers which can reduce the side reaction between Si and the electrolyte, they would be useful as LIB anodes.

Electrochemical performances of chemically etched (30 min) Al–Si and thermally oxidized Si/ $\text{Al}_2\text{O}_3$  foam electrodes were tested in the potential range of 0.005–2.0 V (versus Li/Li<sup>+</sup>) in a coin-type half cell (2016R). Figure 3.10a shows the first cycle voltage profiles of the etched Al–Si and thermally oxidized Si electrodes obtained at the C/20 rate. The etched Si–Al electrodes showed a high charge capacity of 1953 mA h g<sup>-1</sup> in the first cycle, because both Si and Al (a theoretical capacity of 993 mA h g<sup>-1</sup> with composition of LiAl)<sup>22</sup> contribute to the specific capacity. In contrast, the Si/ $\text{Al}_2\text{O}_3$  electrodes thermally oxidized for 10, 30, and 60 min exhibit 1384 (ICE = 83.1%), 1047 (ICE = 82.6%), and 843 mA h g<sup>-1</sup> (ICE = 82.1%), respectively. This is attributed to the increase of inactive  $\text{Al}_2\text{O}_3$  contents in the Si/ $\text{Al}_2\text{O}_3$  particles at the increased oxidation times. Also, the ICE value with increasing oxidation time gradually decreases due to the insulating properties of  $\text{Al}_2\text{O}_3$  layers.

All Si/ $\text{Al}_2\text{O}_3$  electrodes showed a lower specific capacity compared to the etched Al–Si electrodes. However, the Si/ $\text{Al}_2\text{O}_3$  electrodes exhibited outstanding cycling stability at a rate of C/5 until 150 cycles (Figure 3.10b). The etched Al–Si electrode showed fast capacity fading and a poor coulombic efficiency per cycle. It may be attributed to serious side reactions of Si/electrolyte and Al/electrolyte.<sup>22</sup> On the contrary, the Si/ $\text{Al}_2\text{O}_3$  electrodes oxidized for 10, 30, and 60 min exhibit 854, 683, and 628 mA h g<sup>-1</sup> after 150 cycles, respectively, which correspond to capacity retentions of 79%, 84%, and 93% compared to initial capacity. In particular, the 10 min-oxidized Si/ $\text{Al}_2\text{O}_3$  electrode showed excellent long-term cycling stability (a capacity retention of 78% after 300 cycles at the C/5 rate) (Figure 3.10c).

The effect of the  $\text{Al}_2\text{O}_3$  layer on the electrochemical properties can also be identified by electrochemical impedance spectroscopy (EIS) analyses of first-cycled and 120-cycled electrodes (Figure 3.11). EIS spectra of all electrodes did not show any semicircles due to a thin SEI layer and low charge transfer resistance at the first cycle. However, after 120 cycles, the etched Al–Si electrode showed larger SEI and charge transfer resistance than the other oxidized Si/ $\text{Al}_2\text{O}_3$  electrodes. This result indicates that the  $\text{Al}_2\text{O}_3$  protective layer promotes the formation of a stable SEI layer on the Si surface.

Moreover, we tested the rate capabilities of the etched Al–Si and the oxidized Si/ $\text{Al}_2\text{O}_3$  electrodes with various delithiation rates (from C/5 to 10C) at a fixed lithiation rate of C/5. The etched Al–Si electrode showed a large capacity drop from 1525 mA h g<sup>-1</sup> at 0.2C to 269 mA h g<sup>-1</sup> at 10C and did not recover initial specific capacity after 70 cycles. In contrast, thermally oxidized Si/ $\text{Al}_2\text{O}_3$  electrodes exhibited excellent rate capabilities (10 min: a capacity of 79% at 7C, 30 min: a capacity of 82% at 7C, and 60 min: a capacity of 85% at 7C, compared to capacity at the C/5 rate). Also, these

electrodes recovered their capacity to the initial specific capacity after 70 cycles. In addition to delithiation rate capability, lithiation rate capabilities were tested for all Si-based electrodes (Figure 3.12). The specific capacity of the etched Al–Si electrode quickly decayed at the 3C rate, while the oxidized electrodes (10 min and 30 min) still showed a high capacity of  $\sim 400 \text{ mA h g}^{-1}$  at the 3C rate. From the XRD shown in Figure 3.6, we estimated the remaining Al contents. Samples oxidized for 10 min, 30 min, and 60 min still contained the remaining Al contents of 11%, 10%, and 9%, respectively, compared to the etched Al–Si particles. However, most Al thin layers except for the core region are converted to amorphous  $\text{Al}_2\text{O}_3$  layers. Since the Si/ $\text{Al}_2\text{O}_3$  foam with a thin  $\text{Al}_2\text{O}_3$  layer has sponge-like structure in the shell region (except for the Al-rich core region), the rate capability of this electrode is not affected too much depending on the thermal oxidation time. These results indicate that thin  $\text{Al}_2\text{O}_3$  protecting layers prevent side reaction of the nano-sized Si frame in the foam and allow fast transport of lithium ions.

Volume expansion of Si-based electrodes during repeated cycles is one of the critical issues. After the long-term cycling test of the etched Al–Si and the oxidized Si/ $\text{Al}_2\text{O}_3$  electrodes, volume expansion of the electrodes was measured (Figure 3.13). As expected, all oxidized electrodes showed remarkably reduced volume expansion, compared to the Al–Si. Presumably,  $\text{Al}_2\text{O}_3$  protection layers with good mechanical properties and many void spaces in the foam can act as buffers for the large volume change of Si electrodes. To further characterize the stable structural integrity of the oxidized Si/ $\text{Al}_2\text{O}_3$  particles, we measured SEM and TEM of the etched Al–Si and the Si/ $\text{Al}_2\text{O}_3$  electrodes after 120 cycles. The etched Al–Si electrode showed a serious destruction of the original spherical shape of the particle due to a large volume change, while the oxidized sample retained the original shape with suppressed volume change (Figure 3.14).

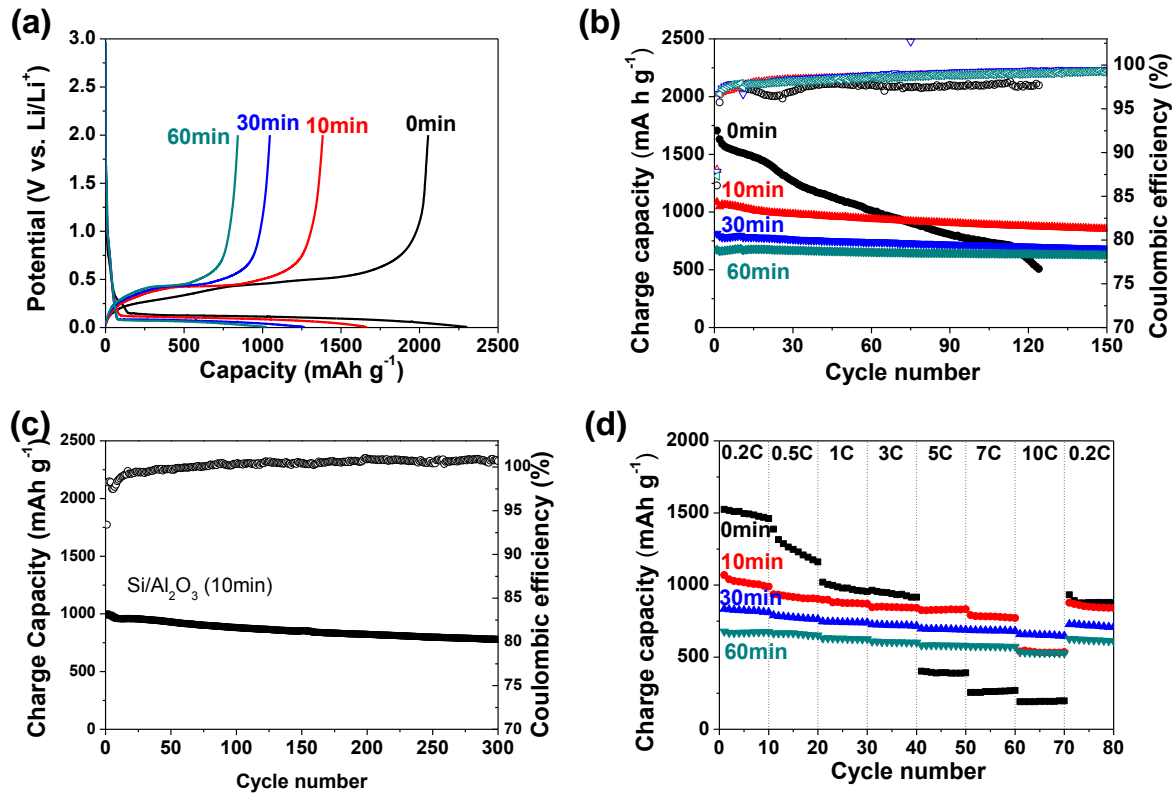


**Figure 3.10.** Electrochemical performances of etched Al-Si and thermally oxidized (10, 30, and 60 min) Si/Al<sub>2</sub>O<sub>3</sub> electrode. (a) First cycle voltage profiles obtained at the C/20 rate and (b) cycling performances at the C/5 rate for four Si-based electrodes. (c) Long-term cycling stability of the thermally oxidized (10 min) Si/Al<sub>2</sub>O<sub>3</sub> electrode. (d) Rate capabilities of four Si-based electrodes obtained in the range of C/5–10C (the lithiation rate was fixed at C/5).

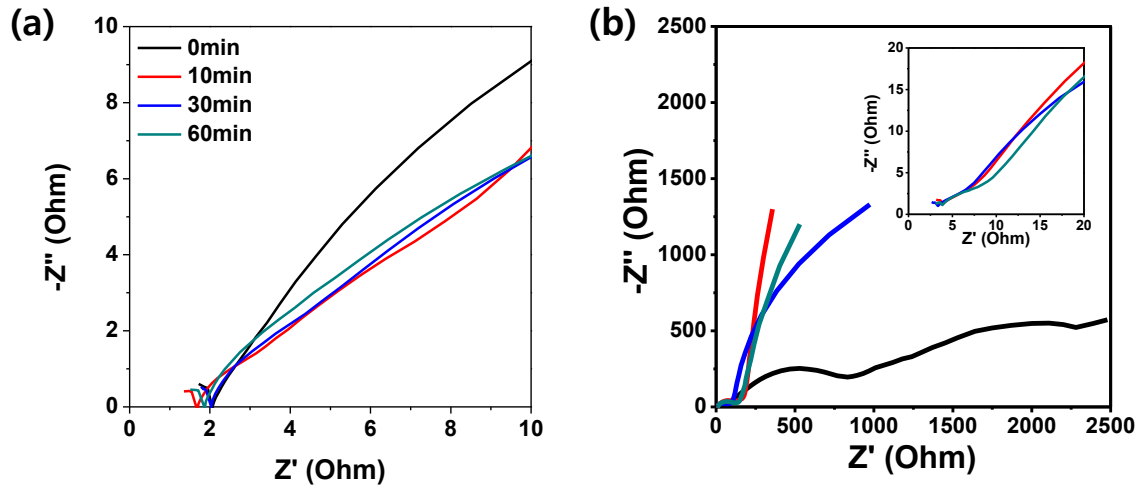


**Figure 3.11.** Electrochemical impedance spectra of chemically etched Al-Si and Si/Al<sub>2</sub>O<sub>3</sub> electrodes thermally oxidized for 10, 30 and 60 min (a) after 1st cycle (b) after 120th cycle.

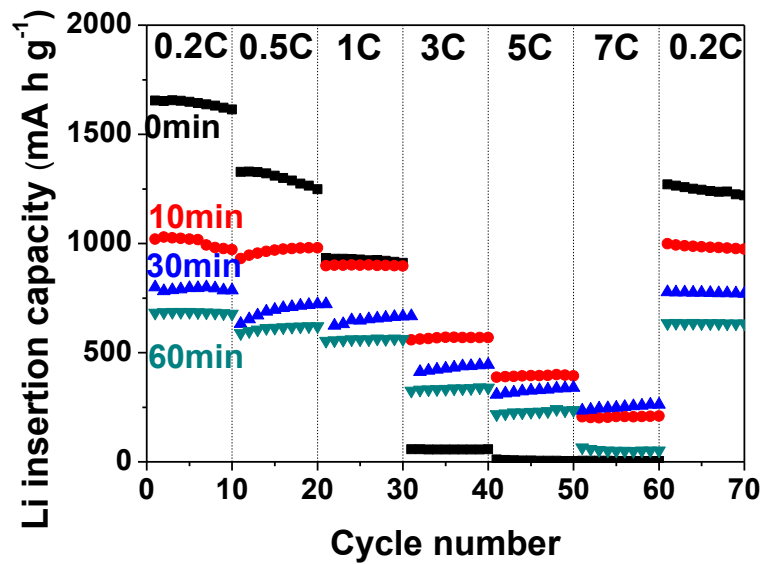


**Figure 3.12.** Rate capabilities of chemically etched Al-Si and Si/Al<sub>2</sub>O<sub>3</sub> electrodes thermally oxidized for 10, 30, and 60 min. The Li extraction rate was fixed at C/5 and Li insertion rate was varied from C/5 to 10C.

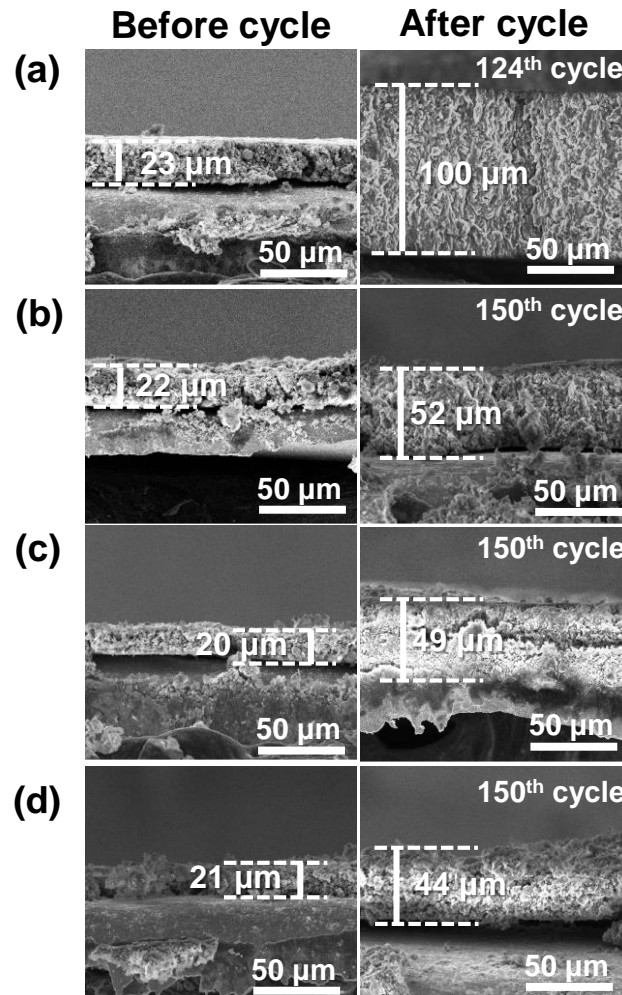


**Figure 3.13.** Cross-sectional SEM images of electrode before and after cycle. (a) Chemically etched Al-Si electrode after 124th cycle and Si/Al<sub>2</sub>O<sub>3</sub> electrodes thermally oxidized for (b) 10 min, (c) 30 min, and (d) 60 min after 150th cycle.

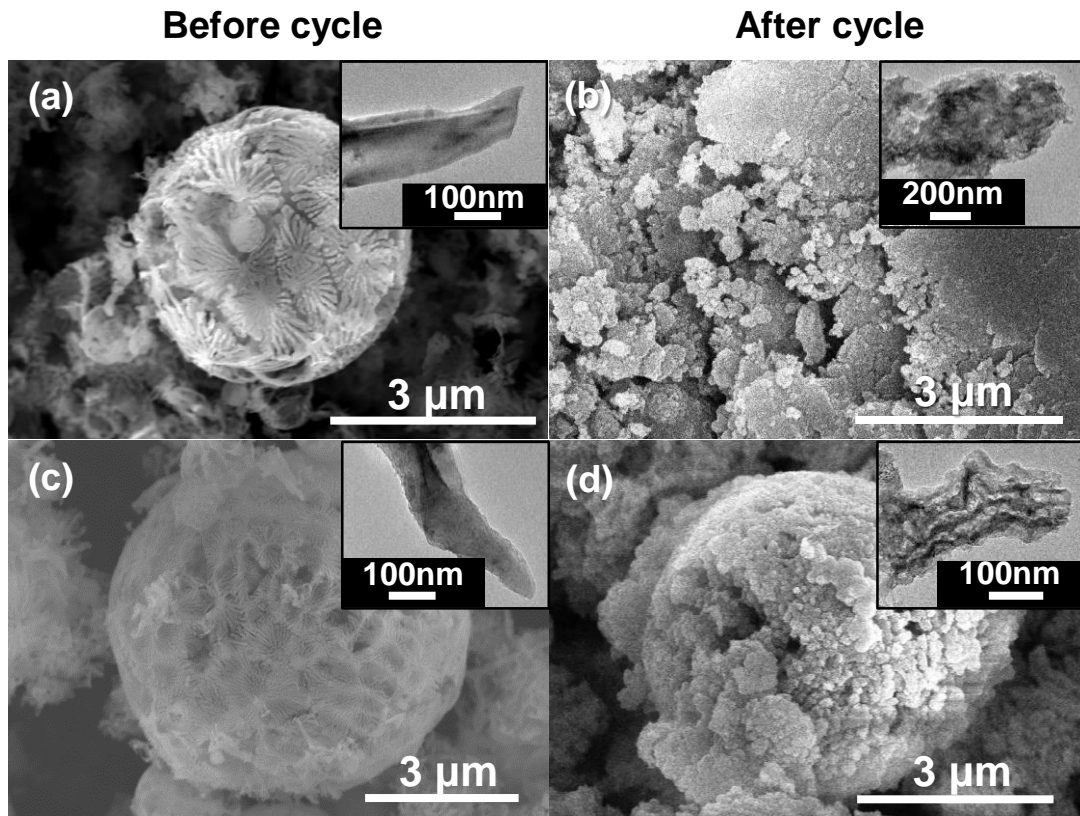


**Figure 3.14.** SEM images of (a) 30 min-chemically etched Al-Si powder before and (b) after 120 cycles. Inset shows the corresponding TEM image of Al-Si frame before and after cycle. SEM images of 10 min-oxidized Si/Al<sub>2</sub>O<sub>3</sub> particles (c) before and (b) after 120 cycles. The corresponding TEM image of Si/Al<sub>2</sub>O<sub>3</sub> frame was seen in the inset before and after cycle.



#### 4. Conclusion

In summary, Si/Al<sub>2</sub>O<sub>3</sub> foam particles were simply synthesized by the chemical etching of the Al–Si alloy and a subsequent selective thermal oxidation process. The Si/Al<sub>2</sub>O<sub>3</sub> electrodes with tunable Al<sub>2</sub>O<sub>3</sub> thickness exhibited highly stable cycling performance, excellent rate capability, and suppressed volume expansion. This strategy opens up an effective way to introduce various protecting layers on the surface of other inorganic materials.

## 5. References

1. U. Kasavajjula, C. Wang and A. J. Appleby, Nano- and bulk-silicon-based insertion anodes for lithium-ion secondary cells. *J. Power Sources* **2007**, *163* (2), 1003-1039.
2. H. Jung, Amorphous silicon anode for lithium-ion rechargeable batteries. *J. Power Sources* **2003**, *115* (2), 346-351.
3. L. Hu, H. Wu, S. S. Hong, L. Cui, J. R. McDonough, S. Bohy and Y. Cui, Si nanoparticle-decorated Si nanowire networks for Li-ion battery anodes. *Chem. Commun.* **2011**, *47* (1), 367-369.
4. C. K. Chan, R. Ruffo, S. S. Hong, R. A. Huggins and Y. Cui, Structural and electrochemical study of the reaction of lithium with silicon nanowires. *J. Power Sources* **2009**, *189* (1), 34-39.
5. M.-H. Park, M. G. Kim, J. Joo, K. Kim, J. Kim, S. Ahn, Y. Cui and J. Cho, Silicon Nanotube Battery Anodes. *Nano Lett.* **2009**, *9* (11), 3844-3847.
6. S. H. Ng, J. Wang, D. Wexler, S. Y. Chew and H. K. Liu, Amorphous Carbon-Coated Silicon Nanocomposites: A Low-Temperature Synthesis via Spray Pyrolysis and Their Application as High-Capacity Anodes for Lithium-Ion Batteries. *J. Phys. Chem.* **2007**, *111*, 11131-11138.
7. C. K. Chan, H. Peng, G. Liu, K. McIlwrath, X. F. Zhang, R. A. Huggins and Y. Cui, High-performance lithium battery anodes using silicon nanowires. *Nat. Nanotechnol.* **2007**, *3* (1), 31-35.
8. W. Zhou, T. Jiang, H. Zhou, Y. Wang, J. Fang and M. S. Whittingham, The nanostructure of the Si–Al eutectic and its use in lithium batteries. *MRS Commun.* **2013**, *3* (03), 119-121.
9. Z. Jiang, C. Li, S. Hao, K. Zhu and P. Zhang, An easy way for preparing high performance porous silicon powder by acid etching Al–Si alloy powder for lithium ion battery. *Electrochim. Acta* **2014**, *115*, 393-398.
10. M. Yoshio, H. Wang, K. Fukuda, T. Umeno, N. Dimov and Z. Ogumi, Carbon-Coated Si as a Lithium-Ion Battery Anode Material. *J. Electrochem. Soc.* **2002**, *149* (12), A1598.
11. S. Yoo, J.-I. Lee, S. Ko and S. Park, Highly dispersive and electrically conductive silver-coated Si anodes synthesized via a simple chemical reduction process. *Nano Energy* **2013**, *2* (6), 1271-1278.
12. S. Sim, P. Oh, S. Park and J. Cho, Critical thickness of SiO<sub>2</sub> coating layer on core@shell bulk@nanowire Si anode materials for Li-ion batteries. *Adv. Mater.* **2013**, *25* (32), 4498-4503.
13. O. Park, J.-I. Lee, M.-J. Chun, J.-T. Yeon, S. Yoo, S. Choi, N.-S. Choi and S. Park, High-performance Si anodes with a highly conductive and thermally stable titanium silicide coating layer. *RSC Adv.* **2013**, *3* (8), 2538.
14. H. Park, S. Lee, S. Yoo, M. Shin, J. Kim, M. Chun, N. S. Choi and S. Park, Control of Interfacial

- Layers for High-Performance Porous Si Lithium-Ion Battery Anode. *ACS Appl. Mater. Interfaces* **2014**, *6* (18), 16360-16367.
15. Y. Yao, N. Liu, M. T. McDowell, M. Pasta and Y. Cui, Improving the cycling stability of silicon nanowire anodes with conducting polymer coatings. *Energy Environ. Sci.* **2012**, *5* (7), 7927.
  16. H. T. Nguyen, M. R. Zamfir, L. D. Duong, Y. H. Lee, P. Bondavalli and D. Pribat, Alumina-coated silicon-based nanowire arrays for high quality Li-ion battery anodes. *J. Mater. Chem.* **2012**, *22* (47), 24618.
  17. Y. He, X. Yu, Y. Wang, H. Li and X. Huang, Alumina-coated patterned amorphous silicon as the anode for a lithium-ion battery with high coulombic efficiency. *Adv. Mater.* **2011**, *23* (42), 4938-4941.
  18. A. M. Goodman and J. M. Breece, Thin Tunnelable Layers of Silicon Dioxide Formed by Oxidation of Silicon. *J. Electrochem. Soc.* **1970**, *117* (7), 982-984.
  19. J. Appenzeller, J. A. d. Alamo, R. Martel, K. Chan and P. Solomon, Ultrathin 600C Wet Thermal Silicon Dioxide. *Electrochem. Solid-State Lett.* **2000**, *3* (2), 84-86.
  20. W. W. Smeltzer, Oxidation of Aluminum in the Temperature Range 400°–600°C. *J. Electrochem. Soc.* **1956**, *103* (4), 209-214.
  21. L. P. H. Jeurgens, W. G. Sloof, F. D. Tichelaar and E. J. Mittemeijer, Growth kinetics and mechanisms of aluminum-oxide films formed by thermal oxidation of aluminum. *J. Appl. Phys.* **2002**, *92* (3), 1649.
  22. Y. Hamon, T. Brousse, F. Jousse, P. Topart, P. Buvat and D. M. Schleich, Aluminum negative electrode in lithium ion batteries. *J. Power Sources* **2001**, *97-98*, 185-187.

\* Chapter III is reproduced in part with permission of “Hwang, G.; Park, H.; Bok, T.; Choi, S.; Lee, S.; Hwang, I.; Choi, N. S.; Seo, K.; Park, S., A high-performance nanoporous Si/Al<sub>2</sub>O<sub>3</sub> foam lithium-ion battery anode fabricated by selective chemical etching of the Al-Si alloy and subsequent thermal oxidation. *Chem. Commun.*, 2015, *51* (21), 4429-4432.”. Copyright 2015 Royal Society of Chemistry.